

Key Points:

- Structural vergence of thrust wedges may change progressively with the increase of lateral/basal shear stress (τ_s/τ_d) ratio
- Under the condition of one weak décollement, frontward, dual and backward vergence occurred when $\tau_s/\tau_d < 0.09$, $= 0.09$ – 1.15 and > 1.15 , respectively
- ESXFTB can be a product of the single northwestward Mesozoic shortening because their two thrust systems have different τ_s/τ_d ratios

Supporting Information:

Supporting Information may be found in the online version of this article.

Correspondence to:

J. Zhou,
jxzhou@cup.edu.cn

Citation:

Zhou, C., & Zhou, J. (2022). Relationship between lateral/basal shear stress ratio and structural vergence of thrust wedges: Results from analogue modeling and implications for the origin of Eastern Sichuan–Xuefeng fold-thrust belt in South China. *Tectonics*, *41*, e2021TC007035. <https://doi.org/10.1029/2021TC007035>


Received 25 AUG 2021

Accepted 26 FEB 2022

Author Contributions:

Conceptualization: Jianxun Zhou
Funding acquisition: Jianxun Zhou
Investigation: Chao Zhou, Jianxun Zhou
Methodology: Jianxun Zhou
Supervision: Jianxun Zhou
Writing – original draft: Chao Zhou, Jianxun Zhou
Writing – review & editing: Jianxun Zhou

Relationship Between Lateral/Basal Shear Stress Ratio and Structural Vergence of Thrust Wedges: Results From Analogue Modeling and Implications for the Origin of Eastern Sichuan–Xuefeng Fold-Thrust Belt in South China

Chao Zhou^{1,2,3} and Jianxun Zhou^{1,2} 

¹State Key Laboratory of Petroleum Resource and Prospecting, China University of Petroleum, Beijing, China, ²College of Geosciences, China University of Petroleum, Beijing, China, ³Now at Institute of Tibetan Plateau Research, Chinese Academy of Sciences, Beijing, China

Abstract Thrust wedges are common in nature, but not all of their origins can be properly explained by the classic Coulomb wedge theory, which considers only a 2D perspective. A few analogue models, however, revealed that lateral shear stress (inherent in both analogue models and nature) may strongly affect the development of thrust wedges and the lateral/basal shear stress (τ_s/τ_d) ratio might have controlled the structural vergence of thrust wedge, suggesting that origin of thrust wedges needs to be considered from a 3D perspective. The origin of the Eastern Sichuan–Xuefeng fold-thrust belt (ESXFTB), which is characterized by two oppositely vergent thrust systems at different crustal levels and may contain another large purely backward-vergent thrust wedge on the world, is still problematic. Revealing the relationship between τ_s/τ_d ratio and structural vergence may prompt a deep understanding of the origin of thrust wedges as well as the ESXFTB. This relationship, however, is still not very clear due to the lack of systematic experiments. For these reasons, we performed systematic experiments of two types of analogue models under different τ_s/τ_d ratios. Our model results revealed, for the first time, that structural vergence of thrust wedges lying on a weak décollement may progressively change from frontward (when $\tau_s/\tau_d < 0.09$) to dual (when $\tau_s/\tau_d = 0.09$ – 1.15) and then to backward (when $\tau_s/\tau_d > 1.15$) and the two oppositely vergent thrust systems in the ESXFTB can be produced simultaneously by the single northwestward Mesozoic shortening probably due to their apparently different τ_s/τ_d ratios.

1. Introduction

Thrust wedges (or fold-thrust belts) are the most common deformational features occurring in the Earth's crust along the convergent plate boundaries. The great majority of the thrust wedges that have been recognized and explored are dominated by imbricate forethrusts or equivalently by forethrusts and backthrusts (e.g., Davis et al., 1983; Pennock et al., 1989; and see Bonini, 2007 for review), showing a frontward or a dual structural vergence (Figures 1a and 1b). These two types of thrust wedges may be perfectly explained by the Coulomb wedge theory (Dahlen, 1990; Davis et al., 1983) and can be well reproduced by analogue as well as numerical models (e.g., Cotton & Koyi, 2000; Huiqi et al., 1992; Smit et al., 2003; also see Graveleau, et al., 2012 and Buitter, 2012 for review). However, the origin of backward-vergent thrust wedges (dominated by imbricate backthrusts), which are uncommon in nature (such as that in Cascadia, see Figure 1c) and can only be reproduced in a few models under specific conditions (e.g., Bonini, 2007; Gutscher et al., 2001; Zhou et al., 2007, 2016), is difficult to be explained properly by the classic Coulomb wedge theory, which considers only a 2D perspective.

A number of factors have been considered to influence the structural vergence of thrust wedges, such as geometry and strength of backstop (Bonini et al., 2000; Byrne et al., 1993; Lallemand et al., 1994; Rossetti et al., 2002), strength and dip of basal décollement (Dahlen, 1990; Davis et al., 1983; Huiqi et al., 1992; Koyi & Vendeville, 2003; Rossetti et al., 2000; Smit et al., 2003), thickness and strength of brittle overburden (Dahlen, 1990; Davis et al., 1983; Huiqi et al., 1992; Lohrmann et al., 2003; Teixell & Koyi, 2003), brittle overburden/basal shear strength ratio (Bonini, 2001, 2003; Couzens-Schultz et al., 2003), lateral rheological contrast of strata (Bonini, 2007; Cotton & Koyi, 2000), and even the initial surface slope or topography of deformed regions (Marques & Cobbold, 2002, 2006; Pons & Mourgues, 2012). Additionally, some particular factors were thought to be responsible for the origin of backward-vergent thrust wedges, such as landward-dipping and very

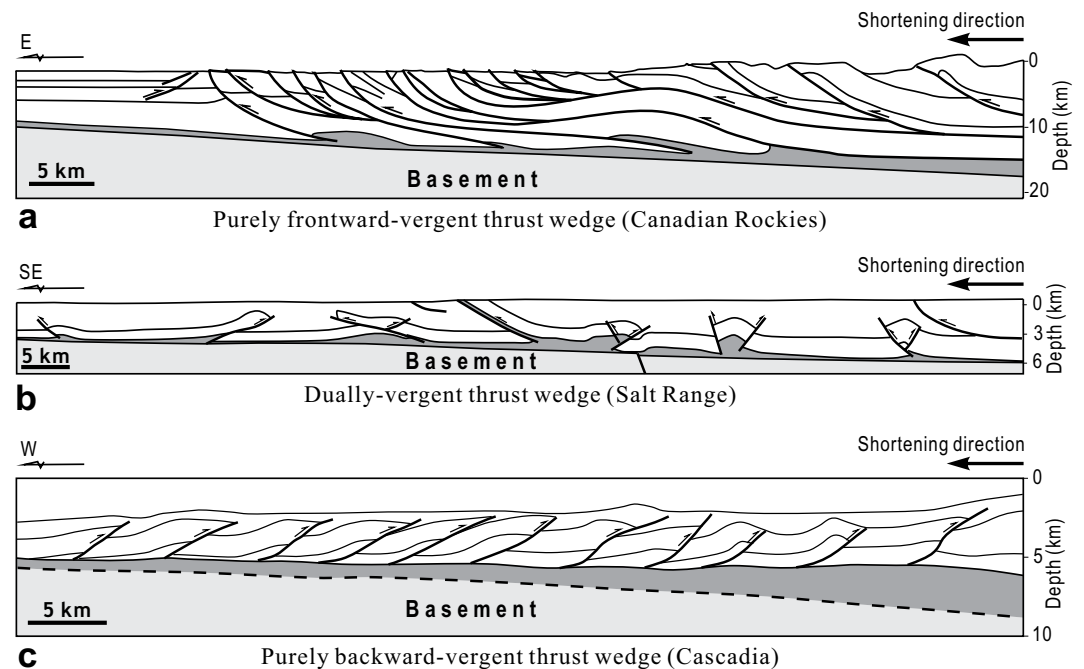


Figure 1. Typical thrust wedges on the world. (a) Purely frontward-vergent thrust wedge in Canadian Rockies (after Davis et al. [1983]). (b) Dually vergent thrust wedge in Salt Range (after Pennock et al. [1989]). (c) Purely backward-vergent thrust wedge in Cascadia (after Gutscher et al. [2001]). Dark layers are weak décollements.

weak basal décollement (e.g., MacKay, 1995; MacKay et al., 1992; Seely, 1977; Tobin et al., 1993; Underwood, 2002; Zhou et al., 2007), seaward-dipping backstop (e.g., Byrne et al., 1993; Byrne & Hibbard, 1987; Gulick et al., 1998; Gutscher et al., 2001), across-strike variation of rheology and reversal of relative shear direction in basal décollement (e.g., Bonini, 2007), as well as specific shortening rates (e.g., Gutscher et al., 2001). Almost all of these considerations are from a 2D perspective and most of the factors proposed for the origin of backward-vergent thrust wedges are difficult to be verified properly by analogue as well as numerical modeling.

Lateral friction exerted by sidewalls of models was generally considered to influence only the portions of models close to the sidewalls and have no substantial effect on the results of entire models in previous studies (e.g., Cotton & Koyi, 2000; Huiqi et al., 1992; Marques & Cobbold, 2002; Smit et al., 2003; Zhou et al., 2007). A few analogue models, however, revealed that both the direction and the magnitude of lateral shear stress (τ_s) on the lateral side of sand layer, exerted by the friction of sidewalls (Costa & Vendeville, 2002, 2004; Souloumiac et al., 2012; Vendeville, 1991, 2007) or by the contiguous blocks due to the lateral rheological contrast (Bonini, 2007; Cotton & Koyi, 2000), may strongly affect or even control the deformation evolution and structural vergence of thrust wedges, especially in the presence of weak décollements. The phenomenon that thrust wedges in nature generally have a curved shape in plain view (e.g., Bahroudi & Koyi, 2003; Cotton & Koyi, 2000) due to the along-strike difference in the velocity of deformation propagation suggests that τ_s is widespread not only in analogue models but also in nature during the development of thrust wedges. Additionally, the fact that analogue models with a same ratio of brittle overburden strength to basal shear strength but with different ratios of τ_s to basal shear stress (τ_d , exerted by the silicone layer or weak décollement on the base of sand layer or brittle overburden) or with different directions of τ_s may have very different structural vergences (Costa & Vendeville, 2002, 2004; Zhou et al., 2016) indicates that the τ_s/τ_d ratio and the direction of τ_s , rather than the brittle overburden/basal shear strength ratio, might have controlled the structural vergence of thrust wedges. Furthermore, the models of Zhou et al. (2016) clearly revealed that: (a) different τ_s directions may cause thrust wedges to be of different or even opposite structural vergences; (b) structural vergence of thrust wedges may change with the τ_s/τ_d ratio; and (c) purely backward-vergent thrust wedges may be formed under the condition of backward-directed τ_s and very high τ_s/τ_d ratio but will disappear from the identical model when the τ_s becomes zero (achieved by removing the sidewalls of the model). All these facts indicate that τ_s may strongly influence or even control the development of thrust wedges and there may be a close relationship between the structural vergence of thrust wedges and the τ_s/τ_d

ratio, not only in analogue models but also in nature. This implies that the origin or dynamics of thrust wedges needs to be considered from a 3D perspective (rather than only from a 2D perspective as in the classic Coulomb wedge theory), as stated by Vendeville (2007): “edge effects (i.e., the effects of τ_s) can strongly influence, or even totally control, the evolution of the entire model, far from the lateral boundaries. The mechanics of a physical model, like that of natural geologic systems, is always three-dimensional.”

However, due to the lack of systematic analogue as well as numerical modeling experiments, the relationship between the structural vergence of thrust wedges and the τ_s/τ_d ratio is still far from being fully understood. The Eastern Sichuan–Xuefeng fold-thrust belt (ESXFTB) located in South China is characterized by two oppositely vergent thrust systems at different crustal levels. Its origin has confused the researchers of this region for many years and has not been proved by analogue or numerical models. Revealing the relationship between the τ_s/τ_d ratio and the structural vergence of thrust wedges may help to understand deeply and provide a universal explanation for the origin or dynamics of all kinds of thrust wedges as well as the ESXFTB, especially those cannot be properly explained by the classic Coulomb wedge theory.

In this study, we conducted systematic analogue experiments to address the aforementioned issues. Our experimental results have successfully revealed that the relationship between the structural vergence of thrust wedges and the τ_s/τ_d ratio and corroborated that lateral shear stress (or friction) condition is a very important factor determining the structures of the entire models, rather than only influencing the portions of models close to the sidewalls.

2. Geologic Setting of the ESXFTB

The Eastern Sichuan–Xuefeng fold-thrust belt (ESXFTB) is located in the middle-upper Yangtze block of South China and comprises four deformation domains, including the Eastern Sichuan, the Western Hunan–Hubei, the Xuefeng, and the Xiangzhong–Lianyuan domains (Figure 2a). It shows a northwestward-convex curvature in plain view and hence is generally considered to be a product of the northwestward shortening that occurred during middle Mesozoic time (He et al., 2018; Yan et al., 2003; Zhang et al., 2013). Additionally, this northwestward-convex curvature suggests the existence of southeastward-directed τ_s on its two lateral boundaries during its northwestward propagation (Figure 2a). The cross section (interpreted from the seismic reflection profile and the surface geology) across its central part shows that it comprises two oppositely vergent thrust systems at its upper and middle crusts (Figure 2b), accompanied by two major weak décollements (Figure 2c), respectively. Its upper crustal thrust system, composed of Upper Archean, Paleozoic, and Triassic strata, is dominated by northwest-directed thrusts, showing a typical northwestward vergence, whereas its middle crustal thrust system, composed of Middle and Lower Archean strata, is occupied almost completely by southeast-directed imbricate thrusts, showing a purely southeastward vergence (Figure 2b). Because the middle crustal thrust system shows a structural vergence opposite to the northwestward Mesozoic shortening direction of this region as well as the structural vergence of the upper crustal thrust system, some researchers argued that the middle crustal thrust system was produced from an earlier tectonic phase, such as the Paleoproterozoic Yangtze–Cathaysia collision (Dong et al., 2015). If this argument is correct, the later northwestward Mesozoic shortening, which had caused intense northwestward thrusting in the upper crustal thrust system, should have evidently left its imprints on the earlier middle crustal thrust system. However, no evidence for such a deformation superimposition can be observed from the cross section (Figure 2b). This implies that the two oppositely vergent thrust systems in the ESXFTB may be the products of the same single northwestward Mesozoic shortening. Thus, in addition to the Cascadia thrust wedge (Figure 1c), the southeastward-vergent middle crustal thrust system of the ESXFTB (Figure 2b) may be another large purely backward-vergent thrust wedge and the ESXFTB may be the first example of large purely backward-vergent thrust wedge accompanied by a frontward-vergent upper thrust system recognized on the world. Although some analogue models have shown apparently different structural vergences between the thrust systems at different levels (e.g., Couzens-Schultz, et al., 2003; Sherkati, et al., 2006), neither analogue nor numerical models shortened from one end has successfully reproduced a structure similar to the ESXFTB (Figure 2b), simultaneously with a purely backward-vergent lower thrust system and a typical frontward-vergent upper thrust system. Therefore, how the single northwestward Mesozoic shortening can produce the ESXFTB and whether the origin of the ESXFTB is due to its different thrust systems having different τ_s/τ_d ratios are still problematic.

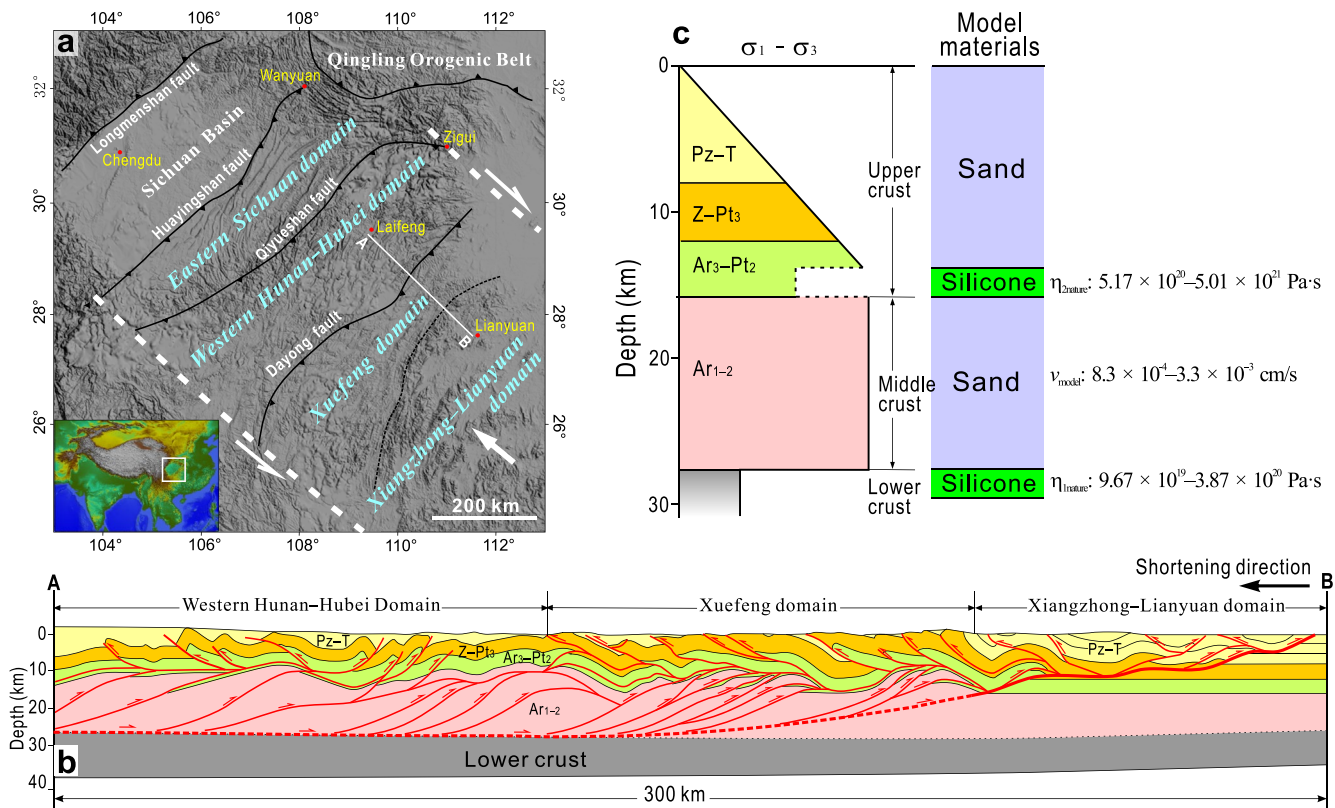


Figure 2. Structural features as well as strata strength profile of the Eastern Sichuan–Xuefeng fold-thrust belt (ESXFTB). (a) USGS Gtopo30 DEM (digital elevation model) map showing the tectonic sketch of the ESXFTB (based on Figure 1 of He et al. [2018]), with the lateral boundaries denoted by two white thick dashed lines. Two white semi-arrows denote the direction of lateral stress and one white arrow denotes the shortening direction. (b) Cross-section across the southeastern part of the ESXFTB (see Figure 2a for location) compiled based on the interpretation of seismic reflection profile in combination with ground geological data (Zhang et al., 2013), showing a typical northwestward structural vergence its upper crustal thrust system and a purely southeastward structural vergence in its middle crustal thrust system. (c) Simplified crustal strength profile of the ESXFTB (based on Dong et al. [2015]; Zhang et al. [2013]) and corresponding analogue materials adopted in the analogue models of this study, showing two major weak décollements lying, respectively, on the top of lower crust and at the bottom of upper crust. Ar = Archean; Pt = Proterozoic; Z = Sinian; Pz = Paleozoic; T = Triassic.

3. Analogue Modeling

Two types of sandbox models with one weak basal décollement (Type A models) and two weak décollements (Type B models), respectively, were designed in this study. The experiments of these models were conducted systematically under a wide range of τ_s/τ_d ratios. The experimental results of them were used to explore the relationship between τ_s/τ_d ratio and structural vergence of thrust wedges in the presence of one weak basal décollement (Type A models) and the origin of the particular structure in the ESXFTB (Type B models), respectively. Considering that the τ_s of models is difficult to be changed significantly (because the frictional coefficient between the quartz sand and the glass sidewall of the models cannot be changed significantly), in this study we chose to change the τ_d of models of to achieve a wide range of the τ_s/τ_d ratios.

3.1. Model Construction and Analogue Materials

In this study, we adopted a 20-cm wide rectangular sandbox rig with the front wall and two glass sidewalls fixed on the steel base plate of the rig. All the models have an initial length of 100 cm and were shortened by 45 cm by moving the back wall inwards, driven by a computer-controlled step motor (Figures 3a and 3b). Thus, the direction of τ_s in these models is opposite to the direction of shortening (Figure 3c). During the experiments, sidewall views of the models were photographed at fixed displacement intervals by a computer-controlled digital camera. All experiments were performed at the Tectonophysics Laboratory of China University of Petroleum in Beijing.

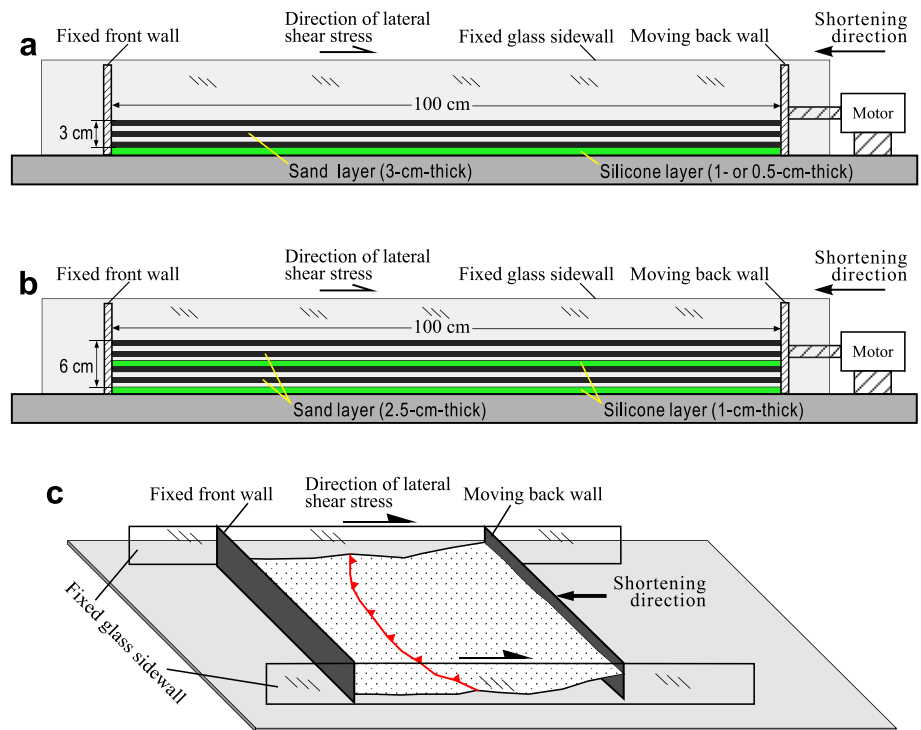


Figure 3. Cross-sectional views of model configurations. (a) Type A models, with a single basal décollement (1- or 0.5-cm-thick) simulated with transparent silicone (green, same in Type B models). (b) Type B models, with two décollements (1-cm-thick) embedded in two 2.5-cm-thick sand layers and lying on the base of model, respectively. The sand layers in all the models have different colors but identical mechanical properties. Note that the direction of lateral shear stress (τ_s , denoted by semi-arrow) in the models is opposite to the direction of shortening (denoted by arrow). (c) 3D illustration of the relationship between the directions of shortening and lateral shear stress in the models, with the width exaggerated by a factor of ~ 4 for clarity.

Dry quartz sand with Mohr-Coulomb behavior and silicone putty with Newtonian fluid behavior have been generally regarded as excellent analogue materials for simulating the frictional behavior of brittle overburdens and the ductile behavior of weak décollements, respectively (e.g., Bonini, 2007; Costa & Vendeville, 2002; Cotton & Koyi, 2000). Dry quartz sand adopted in this study has a grain size of 0.30–0.45 mm, a bulk density of 1.43 g/cm³. Its internal friction coefficient and the frictional coefficient between it and the glass sidewall are 0.65 and 0.15, respectively, both of which were measured with a Hubbert-type shear box. Three types of transparent silicone putty (produced by Guangzhou Shisheng Chemical Ltd of China), which within the range of strain rates in analogue modeling, were adopted to simulate the weak salt or shale décollement (with a density of ~ 2.2 g/cm³) in Type A models and the weak schist décollement in the lower part of Ar₃–Pt₂ formation (with a density of ~ 2.4 g/cm³) and the weak lower crust (with a density of ~ 2.9 g/cm³) in Type B models (see Figure 2c). They have a density of 0.94 g/cm³ and a viscosity (measured by a numerical Brookfield Type viscometer at room temperatures) of 1.77×10^3 Pa·s (silicone 1), 9.47×10^3 Pa·s (silicone 2) and 2.29×10^4 Pa·s (silicone 3), respectively.

3.1.1. Type A Models

This type of models adopted a 3-cm-thick sand layer to simulate brittle overburden, which overlies a 1- or 0.5-cm-thick basal silicone layer (composed of silicone 1 or silicone 3) that simulates a weak basal décollement (Figure 3a). The initial τ_s can be calculated according to the thickness (H_b) and the bulk density (ρ_b) of the sand layer, the frictional coefficient between the sand layer and the glass sidewall (μ_g) and the acceleration of gravity (g), equal to $\rho_b \mu_g (H_b/2)$. Furthermore, the initial τ_d can be calculated according to the shortening velocity of the models (v), the viscosity (η), and the thickness (H_d) of the silicone layer, equal to $v\eta/H_d$ (for details, see Bonini, 2001).

The value of τ_d was changed by varying the value of v , as well as the values of H_d and η in the two end member models ZC22 and ZC12 (Table 1). In the model ZC22, to achieve a very high τ_d of 686.40 Pa, we had to decrease

Table 1
Experimental Parameters of Type A Models

Model	v cm/s	t h	H_b cm	H_d cm	ρ_b g/cm ³	ρ_d g/cm ³	μ_g	η Pa·s	τ_s Pa	τ_d Pa	τ_s/τ_d
ZC22	1.5×10^{-2}	0.83	3	0.5	1.43	0.94	0.15	2.29×10^4	31.53	686.40	0.05
ZC20	1.5×10^{-2}	0.83	3	1	1.43	0.94	0.15	2.29×10^4	31.53	343.20	0.09
ZC19	1.0×10^{-2}	1.24	3	1	1.43	0.94	0.15	2.29×10^4	31.53	225.21	0.14
ZC18	9.2×10^{-3}	1.37	3	1	1.43	0.94	0.15	2.29×10^4	31.53	210.50	0.15
ZC17	8.3×10^{-3}	1.50	3	1	1.43	0.94	0.15	2.29×10^4	31.53	189.90	0.17
ZC16	1.2×10^{-3}	10.38	3	1	1.43	0.94	0.15	2.29×10^4	31.53	27.26	1.15
ZC13	1.0×10^{-3}	12.50	3	1	1.43	0.94	0.15	2.29×10^4	31.53	22.88	1.38
ZC12	1.7×10^{-4}	75.00	3	1	1.43	0.94	0.15	1.77×10^3	31.53	0.30	105.10

Note. v = Shortening velocity; t = Experimental time; H_b = Thickness of the sand layer (brittle overburden); H_d = Thickness of the silicone layer (ductile décollement); ρ_b = Bulk density of the sand layer; ρ_d = Density of the silicone layer; μ_g = Frictional coefficient between the sand layer and the glass sidewall; η = Viscosity of the silicone layer; g = acceleration of gravity; τ_s = Initial lateral shear stress on the sand layer exerted by the sidewall friction, equal to $\rho_b g \mu_g (H_b/2)$; τ_d = Initial basal shear stress on the sand layer exerted by the silicone layer, equal to $v \eta / H_d$.

its H_d to 0.5 cm because its v (1.5×10^{-2} cm/s) has been close to the maximum velocity permission of our deformation device. In the model ZC12, to achieve a very low τ_d of 0.30 Pa and limit the experimental time to a bearable length of 75 hr, we had to decrease its η to 1.77×10^3 Pa·s (otherwise its experimental time would reach an unbearable value of >750 hr and its v would be much less than the minimum velocity permission of our deformation device). Meanwhile, the τ_s of these models remains at 31.53 Pa because it is equal to $\rho_b g \mu_g (H_b/2)$, independent of v . Thus, Type A models were performed under fourteen different τ_s/τ_d ratios, with a wide range from 0.05 to 105.10. In this paper, eight representatives of them were selected for the discussion of the relationship between τ_s/τ_d ratio and structural vergence of thrust wedges in the presence of one weak basal décollement (for details, see Table 1).

3.1.2. Type B Models

According to the crustal strength profile of the ESXFTB (Figure 2c), this type of model adopted two 2.5-cm-thick sand layers to simulate the brittle middle and the upper crusts and two 1-cm-thick silicone layers to simulate the weak décollement lying on the top of lower crust and the weak décollement at the bottom of upper crust composed of schist in the lower part of Ar₃-Pt₂ formation, respectively (Figure 3b). Their lower silicone layer is made up of silicone 1 or silicone 3, while their upper silicone layer is made up of silicone 2 or silicone 3. The initial lateral shear stresses on the lower sand layer (τ_{s1}) and the upper sand layer (τ_{s2}) can be calculated according to the thicknesses of the lower sand layer (H_{b1}) and the upper sand layer (H_{b2}), the thickness of the upper silicone layer (H_{d2}), ρ_b (the bulk density of the sand layer), the bulk density of the silicone layer (ρ_d), the frictional coefficient between the sand layer and the glass sidewall (μ_g) and the acceleration of gravity (g), equal to $\mu_g g [\rho_b (H_{b2} + H_{b1}/2) + \rho_d H_{d2}]$ and $\rho_b g \mu_g (H_{b2}/2)$, respectively. In addition, the initial basal shear stresses on the lower sand layer (τ_{d1}) and the upper sand layer (τ_{d2}) can be calculated according to the shortening velocity of the models (v), the viscosities of the lower silicone layer (η_1) and the upper silicone layer (η_2), and the thicknesses of the lower silicone layer (H_{d1}) and the upper silicone layer (H_{d2}), equal to $v \eta_1 / H_{d1}$ and $v \eta_2 / H_{d2}$, respectively (for details, see Bonini, 2001).

In these models, to achieve different τ_s/τ_d ratios in the two different thrust systems at the same time, the two silicone layers must have different viscosity values (η_1 , η_2). Thus, by varying v of the models (from 1.5×10^{-2} cm/s to 1.7×10^{-4} cm/s) and η_1 and η_2 of the two silicone layers, Type B models were performed under thirteen combinations of different τ_{s1}/τ_{d1} ratios (lower sand layer, ranging from 0.27 to 308.83) and τ_{s2}/τ_{d2} ratios (upper sand layer, ranging from 0.08 to 6.89). In this paper, three representatives of them were selected for the discussion of the origin of the ESXFTB (for details, see Table 2).

Table 2
Experimental Parameters of Type B Models

Model	v cm/s	t h	H_{b1} H_{b2} cm	H_{d1} H_{d2} cm	ρ_b g/ cm ³	ρ_d g/ cm ³	μ_g	η_1 Pa·s	η_2 Pa·s	τ_{s1}/τ_{d1}	τ_{s2}/τ_{d2}
ZC49	3.3×10^{-3}	3.75	2.5	1	1.43	0.94	0.15	1.77×10^3	2.29×10^4	15.86	0.34
ZC47	1.4×10^{-3}	8.83	2.5	1	1.43	0.94	0.15	1.77×10^3	2.29×10^4	37.36	0.81
ZC52	8.3×10^{-4}	15	2.5	1	1.43	0.94	0.15	1.77×10^3	9.47×10^3	68.63	5.00

Note. v = Shortening velocity; t = Experimental time; H_{b1} = Thickness of the lower sand layer (brittle overburden); H_{b2} = Thickness of the upper sand layer (brittle overburden); H_{d1} = Thickness of the lower silicone layer (ductile décollement); H_{d2} = Thickness of the upper silicone layer (ductile décollement); ρ_b = Bulk density of the sand layer; ρ_d = Density of the silicone layer; μ_g = Frictional coefficient between the sand layer and the glass sidewall; η_1 = Viscosity of the lower silicone layer; η_2 = Viscosity of the upper silicone layer; g = acceleration of gravity; τ_{s1} = Initial lateral shear stress on the lower sand layer exerted by the sidewall friction, equal to $\mu_g g [\rho_b (H_{b2} + H_{b1}/2) + \rho_d H_{d2}]$; τ_{s2} = Initial lateral shear stress on the upper sand layer exerted by the sidewall friction, equal to $\rho_b g \mu_g (H_{b2}/2)$; τ_{d1} = Initial basal shear stress on the lower sand layer exerted by the lower silicone layer, equal to $v \eta_1 / H_{d1}$; τ_{d2} = Initial basal shear stress on the upper sand layer exerted by the upper silicone layer, equal to $v \eta_2 / H_{d2}$.

3.2. Model Scaling

3.2.1. Type A Models

The parameters in models and in nature are shown in Table 3. The models may simulate a 3-km-thick and 100-km-long brittle overburden overlying a 0.5- or 1-km-thick weak décollement. The density of brittle overburden (ρ_b) and the density of weak décollement (ρ_d) in nature are taken to be 2.60 g/cm³ and 2.20 g/cm³, respectively, as estimated in Cotton and Koyi (2000). The internal friction coefficient (μ) and cohesion of the brittle overburden (c) in nature are taken to be 0.6–0.85 and ca. 4×10^7 Pa, respectively, as estimated in Bonini (2003). According to Bonini (2007), the viscosity of the weak décollement (η) in nature is assumed to be ca. 10^{19} Pa·s. The cohesion of sand layer (c) in the models is taken to be ca. 80 Pa, as estimated by Bonini (2003). Accordingly, the ratios of model-to-nature for cohesion c^* and stress σ^* were calculated to be 2×10^{-6} and 6×10^{-6} , respectively (Table 3), which are within the same order of magnitude, suggesting that Type A models fulfill a dynamic similarity criterion (Bonini et al., 2012; Cotton & Koyi, 2000). According to the ratio of model-to-nature for strain rate ϵ^* , time t^* and shortening velocity v^* , it is estimated that Type A models may simulate the shortening occurring in nature over 0.25–290 m.y. at a velocity of 0.02–18 cm/yr (Table 3).

Table 3
Scaling Parameters Between Type A Models and Nature

Parameter	Model	Nature	Model/nature ratio (*)
ρ_b (g/cm ³)	1.43	2.60	$\rho_b^* = 0.55$
ρ_d (g/cm ³)	0.94	2.20	$\rho_d^* = 0.43$
μ	0.65	0.6–0.85	$\mu^* = 0.76–1.08$
c (Pa)	80	4×10^7	$c^* = 2 \times 10^{-6}$
η (Pa·s)	$1.77 \times 10^3–2.29 \times 10^4$	10^{19}	$\eta^* = 1.77 \times 10^{-16}–2.29 \times 10^{-15}$
g (m/s ²)	9.81	9.81	$g^* = 1$
l (m)	0.01	1,000	$l^* = 1 \times 10^{-5}$
σ (Pa)	421	7.06×10^7	$\sigma^* = 6 \times 10^{-6}$
ϵ (1/s)	$1.7 \times 10^{-4}–3.0 \times 10^{-2}$	$5.01 \times 10^{-15}–1.15 \times 10^{-11}$	$\epsilon^* = \sigma^*/\eta^* = 2.62 \times 10^9–3.39 \times 10^{10}$
t (h)	0.83–75	$2.17 \times 10^9–2.54 \times 10^{12}$ (0.25–290 m.y.)	$t^* = 1/\epsilon^* = 2.95 \times 10^{-11}–3.82 \times 10^{-10}$
v (cm/s)	$1.7 \times 10^{-4}–1.5 \times 10^{-2}$	$5.01 \times 10^{-10}–5.73 \times 10^{-7}$ (0.02–18 cm/yr)	$v^* = l^*/t^* = 2.62 \times 10^4–3.39 \times 10^5$

Note. μ = Internal friction coefficient of the brittle overburden; c = Cohesion of the brittle overburden; η = Viscosity of the ductile décollement; g = Gravity acceleration; l = Length; σ = Stress (equal to $\rho_b g H_b$); ϵ = Strain rate (equal to v/H_d).

Table 4
Scaling Parameters Between Type B Models and Nature

Parameter	Model	Nature	Model/nature ratio (*)
ρ_{b1} (g/cm ³)	1.43	2.70	$\rho_{b1}^* = 0.53$
ρ_{b2} (g/cm ³)	1.43	2.40	$\rho_{b2}^* = 0.60$
ρ_{d1} (g/cm ³)	0.94	2.90	$\rho_{d1}^* = 0.32$
ρ_{d2} (g/cm ³)	0.94	2.40	$\rho_{d2}^* = 0.39$
μ	0.65	0.6–0.85	$\mu^* = 0.76–1.08$
c (Pa)	80	4×10^7	$c^* = 2 \times 10^{-6}$
g (m/s ²)	9.81	9.81	$g^* = 1$
l (m)	0.01	5,000	$l^* = 2 \times 10^{-6}$
σ (Pa)	794	7.43×10^8	$\sigma^* = 1.07 \times 10^{-6}$
t (h)	3.75–15	8.76×10^{11} (100 m.y.)	$t^* = 4.28 \times 10^{-12}–1.71 \times 10^{-11}$
v (cm/s)	$8.3 \times 10^{-4}–3.3 \times 10^{-3}$	7.1×10^{-9} (0.22 cm/yr)	$v^* = l^*/t^* = 1.17 \times 10^5–4.67 \times 10^5$
ϵ (/s)	$8.3 \times 10^{-4}–3.3 \times 10^{-3}$	1.42×10^{-14}	$\epsilon^* = 1/t^* = 5.85 \times 10^{10}–2.34 \times 10^{11}$
η_1 (Pa·s)	1.77×10^3	$9.67 \times 10^{19}–3.87 \times 10^{20}$	$\eta_1^* = \sigma^*/\epsilon^* = 4.57 \times 10^{-18}–1.83 \times 10^{-17}$
η_2 (Pa·s)	$9.47 \times 10^3–2.29 \times 10^4$	$5.17 \times 10^{20}–5.01 \times 10^{21}$	$\eta_2^* = \sigma^*/\epsilon^* = 4.57 \times 10^{-18}–1.83 \times 10^{-17}$

Note. ρ_{b1} = Density of the lower brittle overburden; ρ_{b2} = Density of upper brittle overburden; ρ_{d1} = Density of the lower ductile décollement; ρ_{d2} = Density of the upper ductile décollement; σ = Stress (equal to $\rho_{b1}gH_{b1} + \rho_{d2}gH_{d2} + \rho_{b2}gH_{b2}$).

3.2.2. Type B Models

Table 4 shows the parameters in models and in nature. The models may simulate two 12.5-km-thick and 500-km-long brittle overburdens, respectively, overlying two 5-km-thick weak décollements. The densities of brittle lower and upper overburdens in nature are taken to be 2.70 g/cm³ (ρ_{b1}) and 2.40 g/cm³ (ρ_{b2}), respectively, and the densities of weak lower and upper décollements in nature are taken to be 2.90 g/cm³ (ρ_{d1}) and 2.40 g/cm³ (ρ_{d2}), respectively, estimated based on Bonini (2003) and Corti et al. (2003). The internal friction coefficient and cohesion of the brittle overburden (μ and c) in nature are estimated to be 0.6–0.85 and 4×10^7 Pa, respectively, and the μ and the c in the models are estimated to be 0.65 and ca. 80 Pa, respectively (same as in Type A models). Accordingly, the ratios of model-to-nature for cohesion c^* and for stress σ^* were calculated to be 2×10^{-6} and 1.07×10^{-6} , respectively, which are within the same order of magnitude, suggesting that Type B models also fulfill a dynamic similarity criterion (Bonini et al., 2012; Cotton & Koyi, 2000). The deformation time in nature is estimated to be ~ 100 m.y. based on He et al. (2018). According to the ratios of model-to-nature for time t^* , for shortening velocity v^* , for strain rate ϵ^* , and for viscosity of weak décollements η^* , it is estimated that Type B models may simulate the middle and the upper crusts with two weak décollements, respectively, of a viscosity $9.67 \times 10^{19}–3.87 \times 10^{20}$ and $5.17 \times 10^{20}–5.01 \times 10^{21}$ that were shortened at a velocity of ~ 0.22 cm/yr for ~ 100 m.y. (Table 4).

3.3. Data Processing

Position and initiation sequence of thrusts in photographs of sequential sidewall views of the models were highlighted by line drawing and numbering, which are used to analyze the deformation evolution and structural vergence of the models. Shortenings accommodated, respectively, by backthrusts and forethrusts in Type A models were measured from the final stage photographs (after 45 cm shortening) of the models, which are used to analyze the change of total shortening accommodated, respectively, by backthrusts and forethrusts with the τ_s/τ_d ratio. According to the displacement increment differences among the pixels of two adjacent sidewall view photographs, fields of the velocity and the strain rate of the models at different shortening stages were derived by MicroVec, a commercial software of PIV (Particle Image Velocimetry) developed by Vision Asia Pte. Ltd. of China (see Adam et al., 2005 for the principle), which may quantitatively illustrate the deformation evolution of the models.

3.4. Limitation of the Analogue Models

In the rear parts of some Type A models with lower τ_s/τ_d ratios (such as models ZC16–20 and ZC22), due to the diapiric rise of silicone layer along the vertical moving back wall and the existence of lateral friction from the glass sidewalls, the sand layers of early emplaced internal units progressively uplifted and slumped over the more external units, showing a slope exceeding the rest angle of the sand in the rear parts of these models (for details, see the results of Type A models shown in Section 4.1). This phenomenon is very dissimilar from natural prototypes but common in many analogue models (e.g., Bonini et al., 2000; Bahroudi & Koyi, 2003; Bonini, 2001, 2003 and 2007). However, all of these models remained their structural vergences throughout their deformation processes. This indicates that this phenomenon has not significantly affected the structural vergence of the models and hence cannot substantially change the conclusions of the relationship between τ_s/τ_d ratio and structural vergence of thrust wedges in this study.

Considering that the thicknesses of the upper and the lower weak décollements in the ESXFTB (Figure 3c) is not well constrained (He et al., 2018), taking 5 km (i.e., 1 cm in the models) for them in Type B models may not exactly reflect the actual conditions. However, because τ_d is a function of ν , η , and H_d (equal to $\nu\eta/H_d$), rather than only the thickness of décollement, this simplification of décollement thicknesses in the models may not substantially affect the discussion of the relationship between the τ_s/τ_d ratio and the structural vergence of the ESXFTB. Erosion and synshortening sedimentation were not taken into account in our models because they generally do not cause substantial changes in structural vergence, although they may influence the deformation evolution of thrust wedges to a certain extent (e.g., Cruz et al., 2010; Persson & Sokoutis, 2002; Smit et al., 2010).

Additionally, different from the condition in nature, the lower silicone layer in Type B models, which simulates the lower weak décollement on the top of lower crust, has a density lower than the overlying sand layer that simulates the brittle middle crust (Figure 2c). In principle, this density inversion in the models could induce the diapiric emplacement of silicone layer into the overlying sand layer and hence change the deformation behavior of the silicone layer. However, the lower silicone layer in the models shows no apparent diapirism and its deformation is still dominated by horizontal shearing (for details, see the results of Type B models shown in Section 4.2), similar to that of its prototype (Figure 2b). Therefore, this technical expedient in the density of analogue material has no significant influence on the deformation behavior of the lower silicone layer and hence may not substantially affect the results of Type B models.

4. Modeling Results

Similar to most of the previous models with homogeneous brittle overburdens and décollements (e.g., Bonini, 2001; Borderie et al., 2018; Costa & Vendeville, 2002; Cubas et al., 2010; Marques & Cobbold, 2002; Smit et al., 2003; Zhou et al., 2016), all of these models show no apparent along-strike differences in structural vergence except for a slightly frontward-convex curvature (see Figure S1a in Supporting Information S1 for example), suggesting that sidewall views of the models can well represent the deformation features of the entire models. Key models of this study were repeated for two to three times to demonstrate the experimental reproducibility and similar results were obtained (see Figure S1b–S1d in Supporting Information S1 for examples).

4.1. Type A Models

The eight representatives (Table 1) of Type A models clearly show progressive change in the structural vergence as well as the development of thrust wedges with the increase of τ_s/τ_d ratio.

4.1.1. Frontward-Vergent Models

Both, models ZC22 and ZC20 with a τ_s/τ_d ratio of 0.05 and 0.09, respectively (Table 1), show a frontward structural vergence.

Model ZC22 ($\tau_s/\tau_d = 0.05$)

Deformation initiated with the formation of forethrusts in front of the moving back wall (Figure 4a). As shortening proceeded, new forethrusts developed forward in-sequence (Figures 4b–4e). As the shortening increased from 9 cm to 45 cm, this model showed a gradual increase in the length and height of thrust wedge, from 17.6

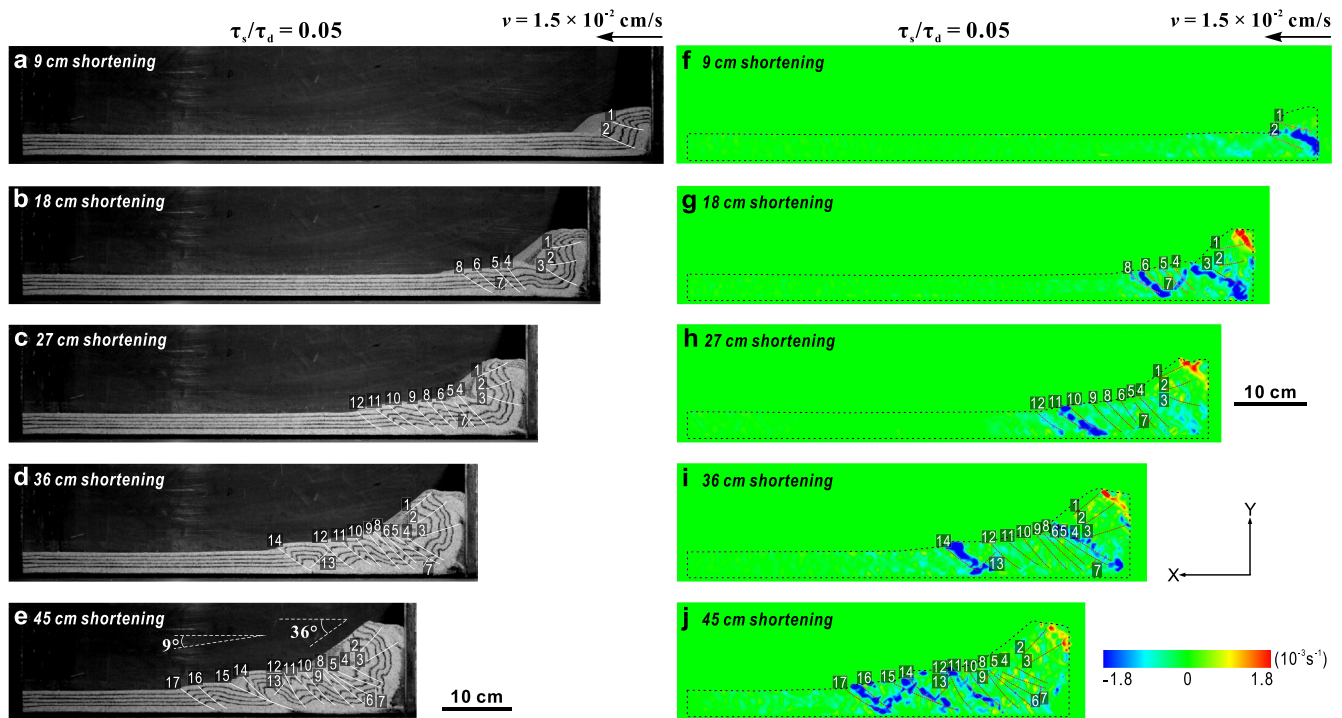


Figure 4. Sequential sidewall views and rate fields of linear strain in X-direction (obtained from PIV analysis, with the black dashed lines showing the outlines of models same in Figures 7 and 8) of Type A model ZC22 at different shortening stages, showing the evolutions of deformation features and high strain rate zones with the increase of shortening. Numbering denotes the initiation sequence of thrusts (same in the following figures). After 45 cm shortening, this model is dominated by in-sequence forward developed forethrusts, showing a typical frontward-vergent thrust wedge with two significantly different topographic slopes of 9° and 36° , respectively, in its front and its rear parts.

to 39.4 cm and from 8.0 to 13.7 cm, respectively (Figure S2a in Supporting Information S1). However, due to diapiric rise of silicone layer along the vertical moving back wall, the rear part of sand layer progressively uplifted and rotated forward, leading to dip direction reverse of some earlier faults (e.g., F1, F2, and F3 in Figure 4d) and slumping of some surface sand (Figures 4b–4e). Additionally, due to the existence of lateral friction (exerted by the glass sidewalls), the slumped sand usually maintained a slope ($\sim 36^\circ$) exceeding the rest angle ($\sim 33^\circ$) of the sand (Figure 4e). Similar phenomena can also be observed in some Type A models with lower τ_s/τ_d ratios (e.g., models ZC16–20) as well as in some previous models (e.g., Bahroudi & Koyi, 2003; Bonini et al., 2000; Bonini, 2001, 2003 and 2007).

As shortening increased, the high rate zone of linear strain (HRZLS) in X-direction, which may better illustrate the strain strength of thrusts (especially those with a dip angle less than 45°), shifted progressively forward in an in-sequence manner. At the stage of 9 cm shortening, one major HRZLS occurred at the toe of the moving back wall (Figure 4f). When the model underwent 18 cm shortening, two new HRZLSs formed along the backthrust 7 and the forethrust 8, respectively, while the early formed HRZLS remained active at the toe of the moving back wall (Figure 4g). As shortening increased to 27 cm, the early formed HRZLSs gradually faded while a new HRZLS formed along the forethrust 11 (Figure 4h). At the stage of 36 cm shortening, the HRZLS at the toe of the moving back wall was reactivated and a new HRZLS formed along the forethrust 14, while the early formed HRZLS along the forethrust 11 faded (Figure 4i). After 45 cm shortening, the HRZLS at the toe of the moving back faded again and the HRZLS along the forethrust was reactivated, while the early formed HRZLS along the forethrust 14 remained active, a new HRZLS formed along the forethrust 17 and a backward-vergent HRZLS formed between the forethrusts 14 and 17 (Figure 4j).

This model is dominated by narrowly spaced thrusts, showing a typical frontward-vergent thrust wedge with two significantly different topographic slopes, 9° in its front part and 36° in its rear part (Figure 4e), an average slope of 14° , a length of 39.4 cm, and a height of 13.7 cm (Figure 5a). The forethrusts and the backthrusts accommodated 23.3% and 1.7% of the total shortening, respectively (Figure 5b), while the rest of the total shortening was

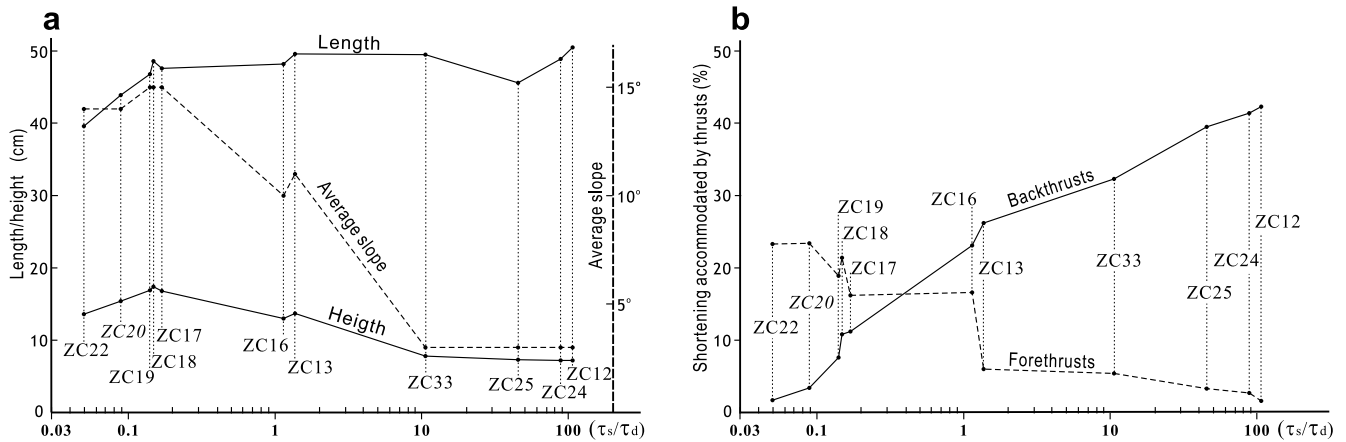


Figure 5. (a) Plots of length, height, and average slope of the thrust wedges vs. τ_s/τ_d ratio in Type A models (measured based on Figures S2–S5 in Supporting Information S1). Note that as the τ_s/τ_d ratio increased, the thrust wedges show a trend of increase in their lengths, while their height and average slope increased first and then decreased as the τ_s/τ_d ratio exceeded 0.17. (b) Plots of the total shortening accommodated, respectively, by backthrusts and forethrusts vs. τ_s/τ_d ratio in Type A models. Note that as the τ_s/τ_d ratio increased, the total shortening accommodated by the forethrusts gradually decreased while the total shortening accommodated by the backthrusts concurrently increased.

accommodated by the folding of sand layer (same in all models). The HRZLSs that are mainly along the forethrusts gathered in the front part of the thrust wedge (Figure 4j).

Model ZC20 ($\tau_s/\tau_d = 0.09$)

Although the τ_s/τ_d ratio of this model is 0.04 higher than that of model ZC22, this model is still dominated by forethrusts that are usually accompanied by a conjugate transient backthrust and have a space wider than those in model ZC22, showing a frontward-vergent thrust wedge with two significantly different topographic slopes, 8° in its front part and 37° in its rear part (Figure 6a), an average slope of 14°, a length of 43.9 cm, and a height of 15.4 cm (Figure 5a). The forethrusts and the backthrusts accommodated 23.4% and 3.4% of the total shortening, respectively (Figure 5b).

4.1.2. Dually Vergent Models

Models ZC19, ZC18, ZC17, and ZC16, which have a τ_s/τ_d ranging from 0.14 to 1.15 (Table 1), show a dual structural vergence.

Model ZC19 ($\tau_s/\tau_d = 0.14$)

Deformation in this model initiated with the formation of forethrusts in front of the moving back wall (Figure 7a). As shortening proceeded, pop-up structures, each of which is bounded by a pair of conjugate forethrust and backthrust, formed forward in-sequence (Figures 7b–7e). When the shortening increased from 9 to 45 cm, the length of thrust wedge in the models gradually increased from 19.8 to 46.8 cm, while the height of that gradually increased from 8.0 to 16.9 cm (Figure S2c in Supporting Information S1).

The HRZLSs in the model progressively shifted forward in-sequence while the early formed ones faded gradually as shortening proceeded. When the models underwent 9 cm shortening, three HRZLSs occurred along the three thrusts in front of the moving back wall (Figure 7f). At the stage of 18 cm shortening, the three early formed HRZLSs gradually faded while two new HRZLSs formed along the backthrust 4 and the forethrust 5, respectively (Figure 7g). As shortening increased to 27 cm, the early formed HRZLSs along thrusts 4 and 5 faded while two new HRZLSs formed along and in front of the forethrust 8, respectively (Figure 7h). As shortening increased further to 36 cm, two new HRZLSs formed along the backthrust 11 and the forethrust 12, respectively, while the two early formed HRZLSs along the thrusts 8 and 10 maintained active, respectively (Figure 7i). After 45 cm shortening, two new HRZLSs formed along the backthrust 13 and the forethrust 14. Meanwhile, except for the HRZLS along the forethrust 12, all of the early formed HRZLSs faded (Figure 7j).

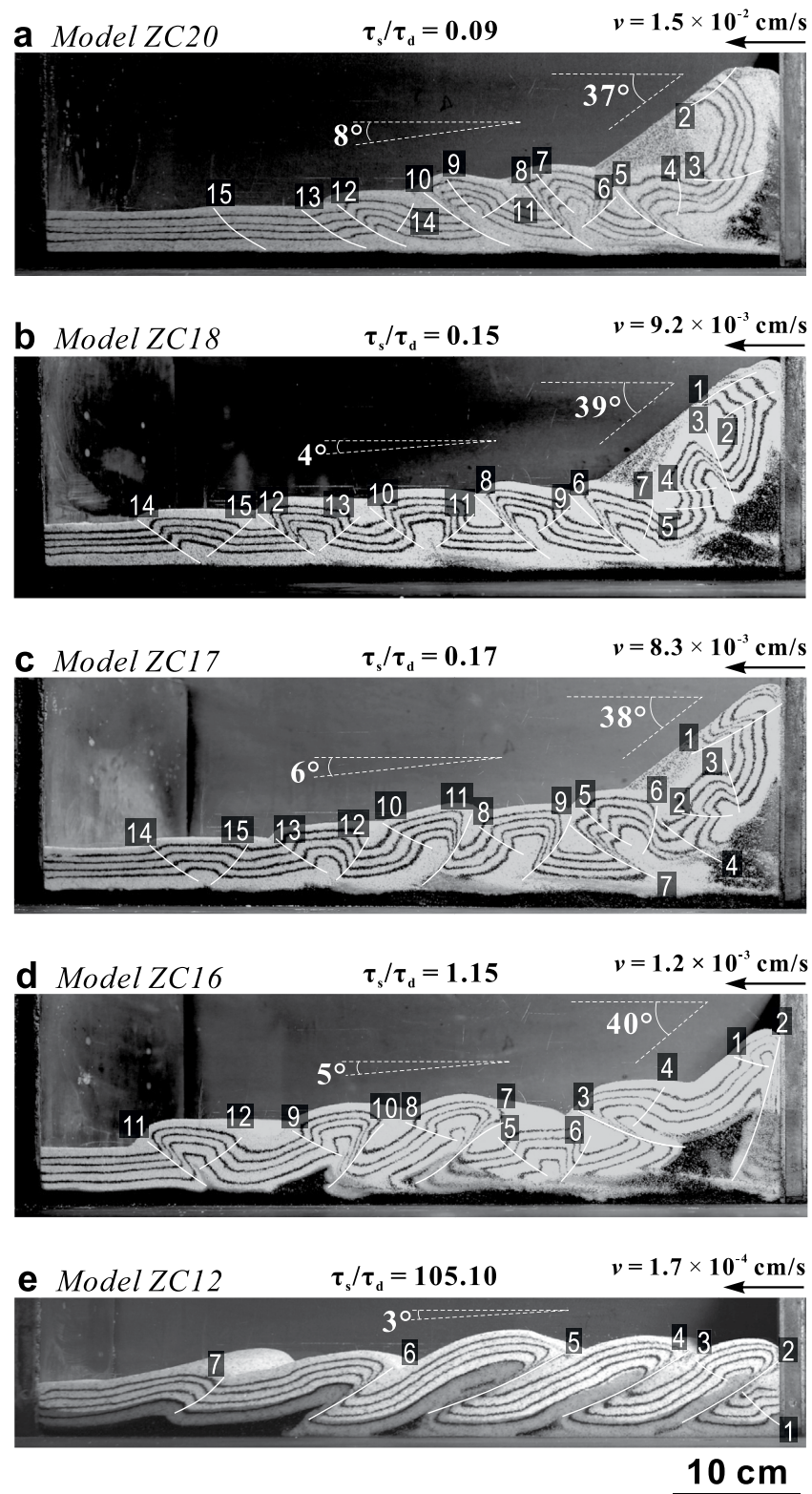


Figure 6.

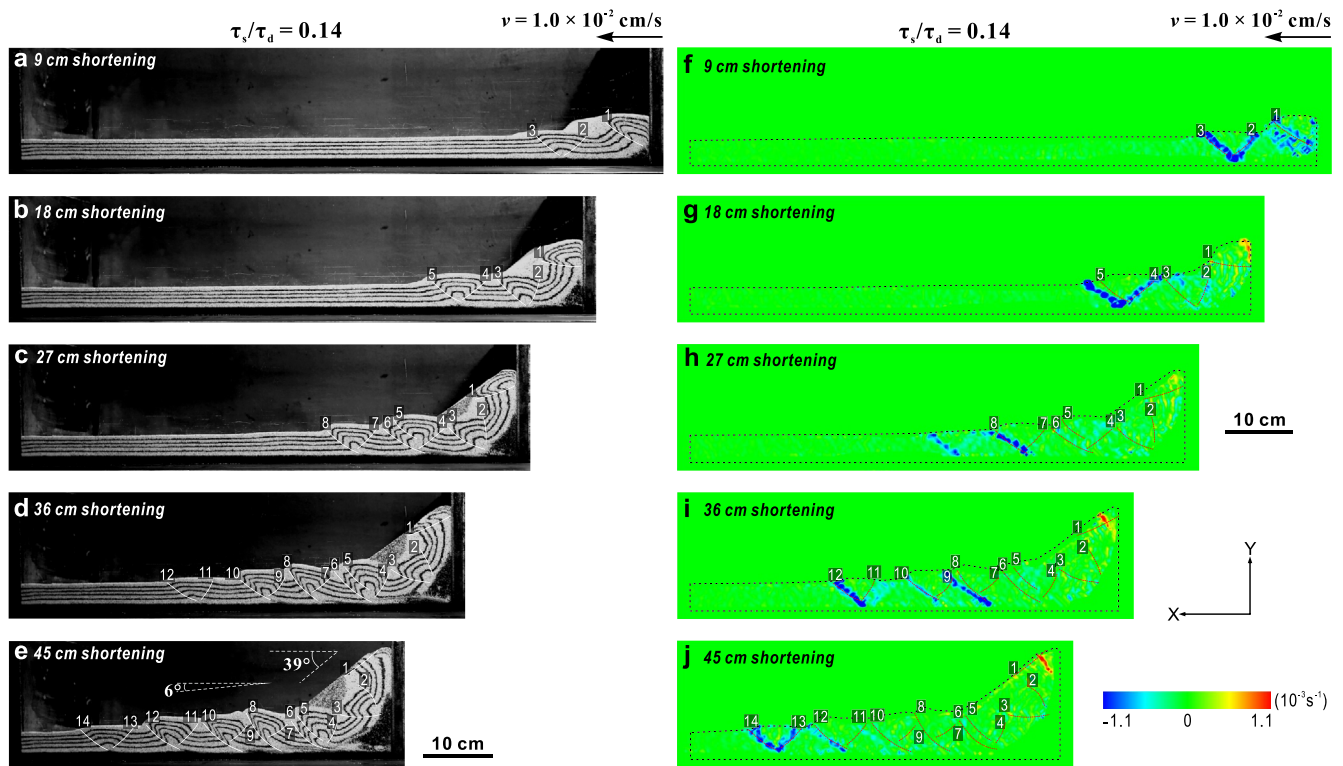


Figure 7. Sequential sidewall views and rate fields of linear strain in X-direction of Type A model ZC19 at different shortening stages, showing the evolutions of deformation features and high strain rate zones with the increase of shortening. After 45 cm shortening, this model is dominated by in-sequence forward developed pop-up structures (bounded by a pair of conjugate forethrust and backthrust, respectively), showing a dually vergent thrust wedge with a frontward preferred vergence and two significantly different topographic slopes of 6° and 39° , respectively, in its front and its rear parts.

This model is dominated by pop-up structures, showing a dually vergent thrust wedge with a frontward preferred structural vergence and two significantly different topographic slopes, 6° in their front parts and 39° in their rear parts (Figure 7e), an average slope of 15° , a length of 46.8 cm and a height of 16.9 (Figure 5a). The forethrusts and the backthrusts accommodated 18.9% and 7.6% of the total shortening, respectively (Figure 5b). The HRZLSs that are along both the forethrusts and backthrusts gathered in the anterior half of the thrust wedge's front part (Figure 7j).

Models ZC18 ($\tau_s/\tau_d = 0.15$), ZC17 ($\tau_s/\tau_d = 0.17$), and ZC16 ($\tau_s/\tau_d = 1.15$)

These three models have a similar deformation process to model ZC19. Models ZC18 and ZC17 are also dominated by pop-up structures (Figures 6b and 6c), while model ZC16 is dominated equivalently by forethrusts and backthrusts, accompanied by a conjugate transient backthrust or forethrust (Figure 6d). They show dually vergent thrust wedges with two significantly different topographic slopes. As the τ_s/τ_d ratio increased, the preferred structural vergence of these models changed gradually from frontward (Figure 7e) to weak frontward (Figure 6b) and then to backward (Figures 6c and 6d). After 45 cm shortening, models ZC18, ZC17 have an average slope of 15° (same as model ZC19), while model ZC16 has an average slope of 10° (Figure 5a). Their front and rear parts have a slope of 4° – 6° and 38° – 40° , respectively (Figures 6b–6d). The thrust wedges in these models have

Figure 6. Sidewall views of Type A models after 45 cm shortening. (a) Model ZC20, dominated by in-sequence forward developed forethrusts, usually accompanied by a conjugate transient backthrust, showing a frontward-vergent thrust wedge with two significantly different topographic slopes of 9° and 36° , respectively, in its front and its rear parts. (b) Model ZC18, dominated by in-sequence forward developed pop-up structures, showing a typical dually vergent thrust wedge with a weak frontward preferred vergence and two significantly different topographic slopes of 4° and 39° , respectively, in its front and its rear parts. (c) Model ZC17, dominated by in-sequence forward developed pop-up structures, showing a dually vergent thrust wedge with a backward preferred vergence and two significantly different topographic slopes of 6° and 38° , respectively, in its front and its rear parts. (d) Model ZC16, dominated by both forethrusts and backthrusts, usually accompanied by a conjugate transient backthrust or forethrust, showing a dually vergent thrust wedge with a backward preferred vergence and two significantly different topographic slopes of 5° and 40° , respectively, in its front and its rear parts. (e) Model ZC12, dominated by in-sequence forward developed backthrusts, showing a purely backward-vergent thrust wedge with a topographic slope of 3° .

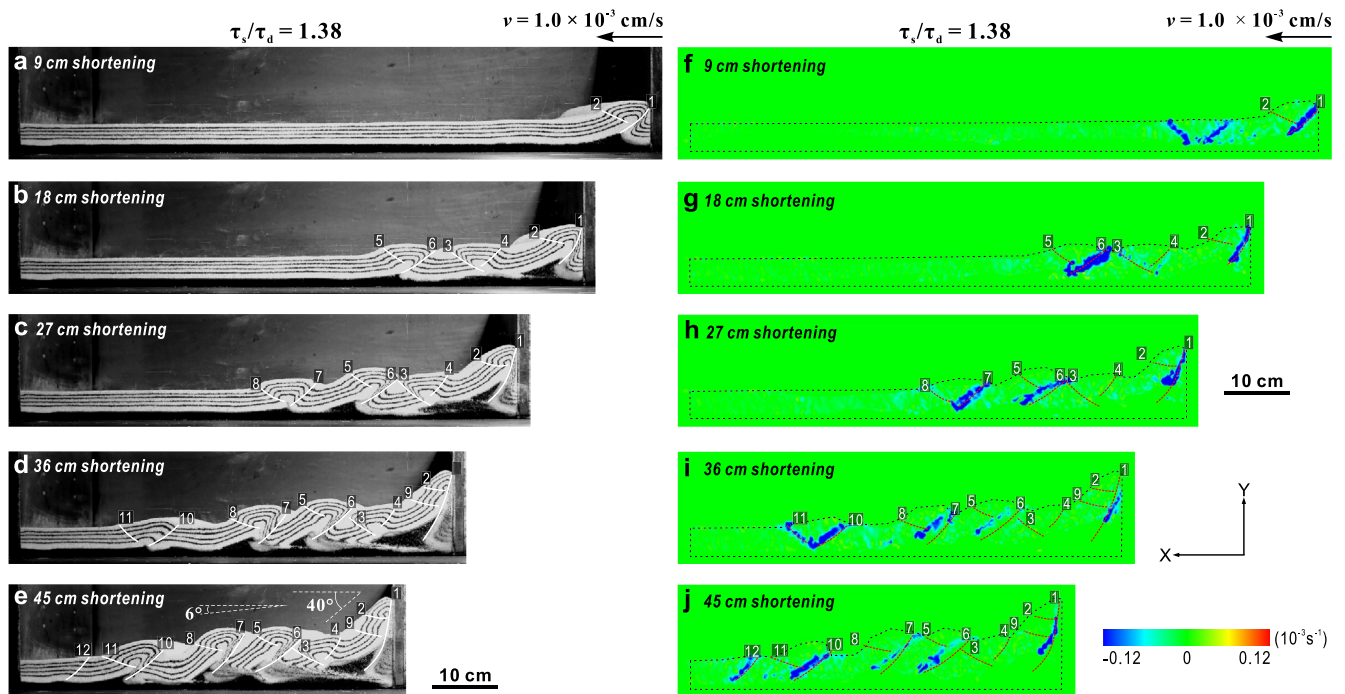


Figure 8. Sequential sidewall views and rate fields of linear strain in X-direction of Type A model ZC13 at different shortening stages, showing the evolutions of deformation features and high strain rate zones with the increase of shortening. After 45 cm shortening, this model is dominated by in-sequence forward developed backthrusts, each of which is accompanied by one or two conjugate transient forethrusts, showing a backward-vergent thrust wedge with two significantly different topographic slopes of 6° and 40° , respectively, in its front and its rear parts.

a length of 46.8–48.6 cm and a height of 16.8–17.4 cm (Figure 5a). The forethrusts and the backthrusts in these models accommodated 21.4% and 10.8% (ZC18), 16.2% and 11.2% (ZC17) and 16.6% and 23.1% (ZC16) of the total shortening, respectively (Figure 5b).

4.1.3. Backward-Vergent Models

Models ZC13, ZC33, ZC25, ZC24, and ZC12, which have a τ_s/τ_d ranging from 1.38 to 105.10 (Table 1; Figures S3–S5 in Supporting Information S1), generally show a backward structural vergence.

$$\text{Model ZC13 } (\tau_s/\tau_d = 1.38)$$

Deformation in this model initiated with the formation of a backthrust accompanied by a conjugate transient forethrust in front of the moving back wall (Figure 8a), followed by a pop-up structure in front of it (Figure 8b). As shortening proceeded, new backthrusts usually accompanied by a conjugate transient forethrust formed in-sequence forward (Figures 8c–8e). As shortening increased from 9 to 45 cm, the length and height of thrust wedge in this model gradually increased from 24.0 to 49.6 cm and from 7.7 to 13.7 cm, respectively (Figure S2g in Supporting Information S1).

With the increase of shortening, the HRZLSs in this model progressively shifted forward in-sequence, while most of the early formed ones maintained their activities (Figures 8f–8j). At the stage of 9 cm shortening, three HRZLSs occurred in front of the moving back wall along the backthrust 1 and the upcoming thrusts 3 and 4 (Figure 8f). As shortening increased to 18 cm, a new HRZLS formed along the backthrust 6, while the two early formed HRZLSs along thrusts 3 and 4 gradually faded and the early formed HRZLS along the backthrust 1 maintained active (Figure 8g). After 27 cm shortening, a new HRZLS formed along the backthrust 7, while the early formed HRZLSs along the backthrusts 1 and 6 maintained their activities (Figure 8h). As shortening increased further to 36 cm, two new HRZLSs formed along the backthrust 10 and the forethrust 11, respectively, while the three early formed HRZLSs, respectively, along the backthrusts 1, 6, and 7 maintained active (Figure 8i). After 45 cm shortening, a new HRZLS formed along the backthrust 12 while the early formed HRZLS along the forethrust 11 faded. All of the early formed HRZLSs along the backthrusts remained active (Figure 8j).

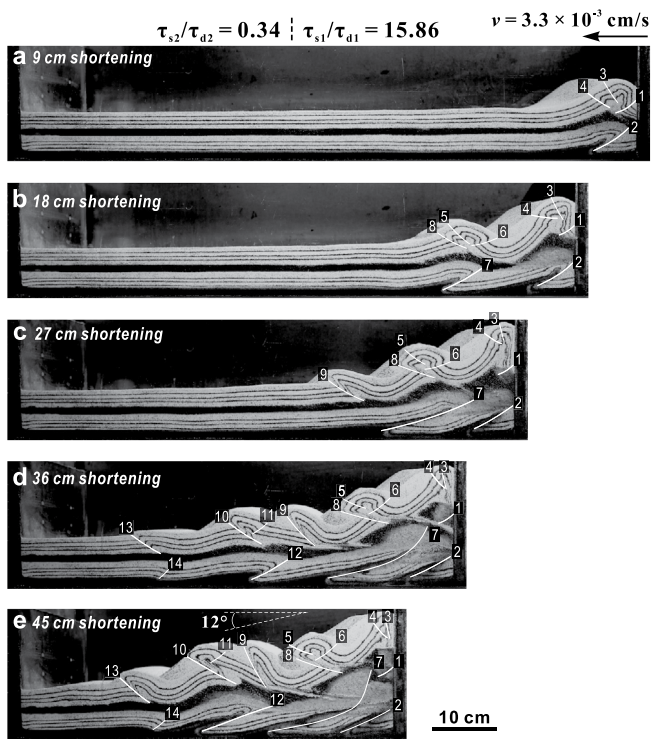


Figure 9. Sequential sidewall views of Type B model ZC49 at different shortening stages. After 45 cm shortening, the lower thrust system of the model is dominated by in-sequence forward developed backthrusts, showing a purely backward-vergent thrust wedge with a taper of $\sim 7^\circ$, while the upper thrust system of the model is dominated by in-sequence forward developed forethrusts, showing a typical frontward-vergent thrust wedge with a topographic slope of $\sim 12^\circ$.

This model is dominated by in-sequence forward developed backthrusts, each of which is accompanied by one or two conjugate transient forethrusts, showing a backward-vergent thrust wedge with two significantly different topographic slopes, 6° in its front part and 40° in its rear part (Figure 8e), an average slope of 11° , a length of 49.6 cm, and a height of 13.7 cm (Figure 5a). The forethrusts and the backthrusts accommodated 6.0% and 26.2% of the total shortening, respectively (Figure 5b). The HRZLSs that are mainly along the backthrusts are distributed over almost the entire range of the thrust wedge (Figure 8j).

Models ZC33 ($\tau_s/\tau_d = 10.48$), ZC25 ($\tau_s/\tau_d = 45.31$),
ZC24 ($\tau_s/\tau_d = 87.60$), and ZC12 ($\tau_s/\tau_d = 105.10$)

As the τ_s/τ_d ratio increased, in these four models the total shortening accommodated by the backthrusts gradually increased, while the total shortening accommodated by the forethrusts decreased further and thus the conjugate transient forethrusts that accompanied the backthrusts gradually disappeared (Figures S3–S5 in Supporting Information S1), resulting in the occurrence of purely backward-vergent thrust wedge (Figure 6e). The total shortenings accommodated by the forethrusts in these four models are 5.4%, 3.3%, 2.7%, and 1.6% and the total shortenings accommodated by the backthrusts are 32.3%, 39.5%, 41.4%, and 42.3%, respectively (Figure 5b). The thrust wedges in these models have a relatively uniform topographic slope of 3° , a length of 49.5, 45.6, 48.9, and 50.5 cm, and a height of 7.8, 7.3, 7.2, and 7.2 cm, respectively (Figure 5a).

4.2. Type B Models

The three representatives (Table 2) of Type B models show that as the τ_s/τ_d ratios increased, the upper thrust system (UTS) of these models changed their structural vergence from frontward (ZC49) to dual (ZC47) and then to backward (ZC52) while their lower thrust system (LTS) remained a purely backward vergence.

4.2.1. Model ZC49 ($\tau_{s2}/\tau_{d2} = 0.34$; $\tau_{s1}/\tau_{d1} = 15.86$)

Deformation in this model initiated in front of the moving back wall, with the formation of a backthrust in its LTS and a backthrust accompanied by two conjugate transient forethrusts in its UTS (Figure 9a). As shortening increased, new backthrusts and forethrusts formed in-sequence forward in the LTS and the UTS, respectively. When the model experienced 18 cm shortening, a new backthrust developed forward in its LTS and two forethrusts with a conjugate transient backthrust formed forward in its UTS (Figure 9b). As shortening increased to 27 cm, a new forethrust formed forward in its UTS, but no new thrust was formed in its LTS (Figure 9c). At the stage of 36 cm shortening, two new backthrusts formed forward in the LTS while two new forethrusts with a conjugate transient backthrust formed forward in the UTS (Figure 9d).

After 45 cm shortening, the thrust wedge in this model has a length of 49.5 cm and a height of 18.5 cm (Figure 10a). The LTS is dominated by backthrusts, showing a purely backward-vergent thrust wedge with an average slope of $\sim 7^\circ$, while the UTS is dominated by forethrusts, showing a typical frontward-vergent thrust wedge with an average slope of $\sim 12^\circ$ (Figures 9e and 10a). The total shortening accommodated, respectively, by forethrusts and backthrusts in the LST is 0% and 53.0%, while that in the UTS is 26.9% and 2.5% (Figure 10b).

4.2.2. Model ZC47 ($\tau_{s2}/\tau_{d2} = 0.81$; $\tau_{s1}/\tau_{d1} = 37.36$)

Deformation in this model initiated in front of the moving back wall, with the formation of a backthrust in both its LTS and its UTS, accompanied by a conjugate transient forethrust (Figures 11a). As shortening increased, new backthrusts, occasionally accompanied by a conjugate transient forethrust, formed in-sequence forward in the LTS, while new forethrusts accompanied by a conjugate transient backthrust or backthrusts accompanied by

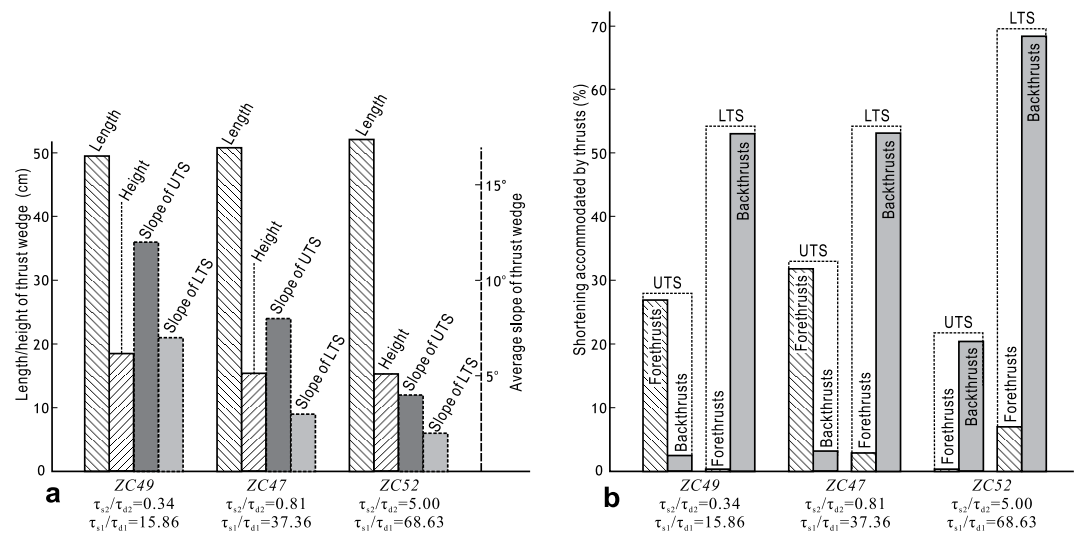


Figure 10. (a) Histograms of length and height of the thrust wedges and average slopes of the upper thrust system (UTS) and the lower thrust system (LTS) in Type B models (measured based on Figures 9, 11 and 12). Note that as the τ_s/τ_d ratio increased, the thrust wedges show a trend of increase in their lengths, while their height and average slopes gradually decreased. (b) Histograms of the total shortening accommodated, respectively, by forethrusts and backthrusts of Type B models. Note that as the τ_s/τ_d ratio increased, the total shortening accommodated by the forethrusts in the LTS and by the backthrusts in both the LTS and the UTS increased.

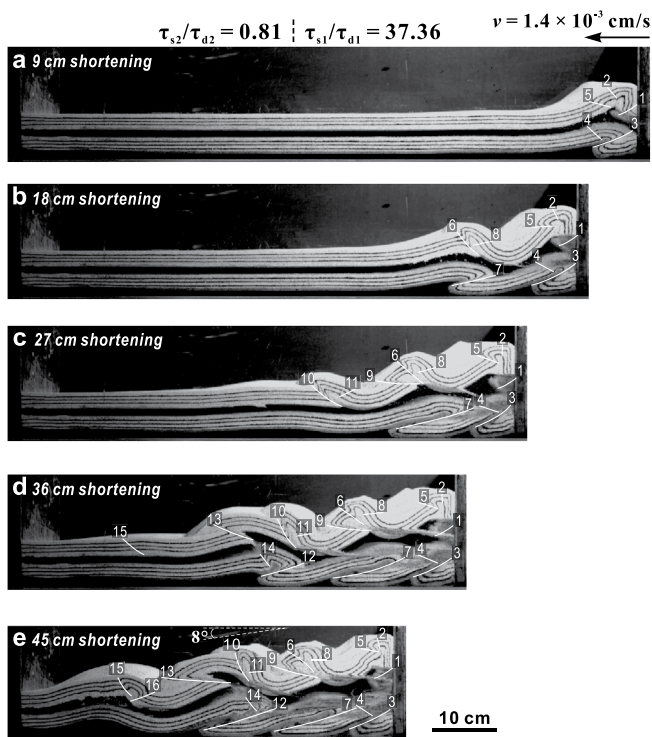


Figure 11. Sequential sidewall views of Type B model ZC47 at different shortening stages. After 45 cm shortening, the lower thrust system of the model is dominated by in-sequence forward developed backthrusts, showing a purely backward-vergent thrust wedge with a taper of $\sim 3^\circ$, while the upper thrust system of the model is dominated equivalently by forethrusts and backthrusts, showing a dually vergent thrust wedge with a topographic slope of $\sim 8^\circ$.

a conjugate transient forethrust formed forward in the UTS. As shortening increased to 18 cm, a new backthrust developed forward in its LTS, while two forethrusts, one of which was accompanied by a conjugate transient backthrust, formed forward in its UTS (Figures 11b). When the model underwent 27 cm shortening, two new forethrusts formed forward in its UTS, one of which was accompanied by a conjugate transient backthrust, but no new thrust was formed in its LTS (Figures 11c). As shortening increased further to 36 cm, one new backthrust accompanied by a conjugate transient forethrust formed forward in the LTS while two new forethrusts formed forward in the UTS (Figures 11d). As shortening increased to 45 cm, one new backthrust accompanied by a forethrust formed forward in the UTS (Figures 11e).

After 45 cm shortening, the thrust wedge in this model has a length of 50.8 cm and a height of 15.4 cm (Figure 10a). The LTS is dominated by backthrusts, showing a purely backward-vergent thrust wedge with an average slope of $\sim 3^\circ$, while the UTS is dominated by forethrusts and backthrusts, showing a dually vergent thrust wedge with a topographic slope of $\sim 8^\circ$ (Figures 11e and 10a). The total shortening accommodated, respectively, by forethrusts and backthrusts in the LST is 2.9% and 53.1%, while that in the UTS is 31.8% and 3.2% (Figure 10b).

4.2.3. Model ZC52 ($\tau_{s2}/\tau_{d2} = 5.00$; $\tau_{s1}/\tau_{d1} = 68.63$)

Deformation in this model initiated in front of the moving back wall, with the formation of a backthrust in both its LTS and its UTS, accompanied by a conjugate transient forethrust in the LTS (Figure 12a). As shortening increased, new backthrusts formed in-sequence forward in both the LTS and the UTS. When the model experienced 18 cm shortening, a new backthrust developed forward in both its LTS and its UTS (Figure 12b). At the stage of 27 cm shortening, one more backthrust formed forward in both its LTS and its UTS (Figure 12c). As shortening increased further to 36 cm, two new backthrusts formed forward in the UTS, but no new backthrust was formed in the LTS (Figure 12d).

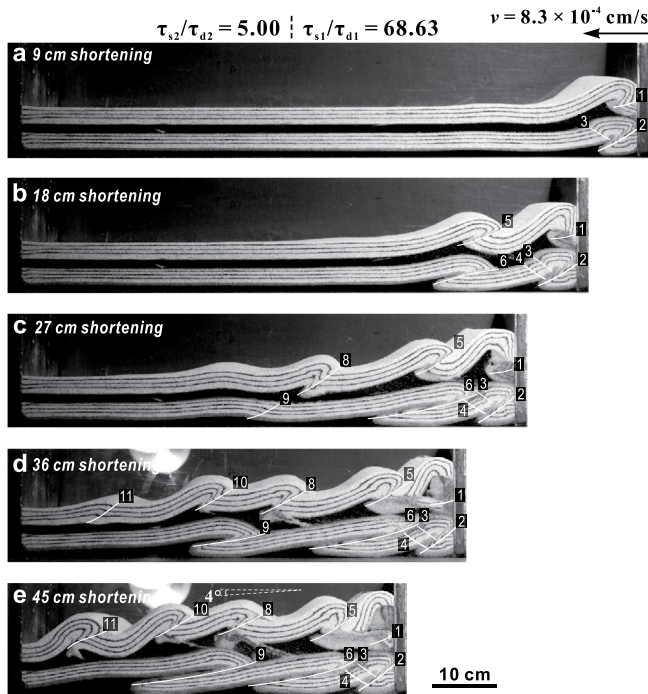


Figure 12. Sequential sidewall views of Type B model ZC52 at different shortening stages. After 45 cm shortening, both the lower and the upper thrust systems of the model are dominated by in-sequence forward developed backthrusts, showing purely backward-vergent thrust wedges with a taper of $\sim 2^\circ$ and a topographic slope of $\sim 4^\circ$, respectively.

After 45 cm shortening, the thrust wedge in this model has a length of 52.1 cm and a height of 15.3 cm (Figure 10a). Both the LTS and the UTS are dominated by backthrusts, showing a purely backward-vergent thrust wedge with an average slope of $\sim 2^\circ$ and $\sim 4^\circ$, respectively (Figures 12e and 10a). The total shortening accommodated, respectively, by forethrusts and backthrusts in the LST is 7.0% and 68.3%, while that in the UTS is 0% and 20.4% (Figure 10b).

5. Discussion

5.1. Relationship Between τ_s/τ_d Ratio and Structural Vergence of Thrust Wedges

Results of our models with a τ_s/τ_d ratio from 0.05 to 105.1 clearly show that the structural vergence of thrust wedges may change with the variation of τ_s/τ_d ratio. This demonstrates that τ_s/τ_d ratio is a key factor determining the structural vergence of thrust wedges and corroborates that the origin or dynamics of thrust wedges needs to be considered from a 3D perspective because τ_s is inherent in both analogue models and nature (Vendeville, 2007). Type A models indicate that in the presence of one weak basal décollement, frontward-, dually and backward-vergent thrust wedges may occur when the $\tau_s/\tau_d < 0.09$, $= 0.09-1.15$, and > 1.15 , respectively, and in particular, purely frontward- and purely backward-vergent thrust wedges may occur when their $\tau_s/\tau_d < 0.05$ and > 105 , respectively (Figure 13a). Generally, as the τ_s/τ_d ratio increased, the thrust wedges show a trend of increase in their lengths, while their height and average slope increased first and then decreased as the τ_s/τ_d ratio exceeded 0.17 (Figure 5a). Meanwhile, the total shortening accommodated by backthrusts may gradually increase, whereas the total shortening accommodated by forethrusts may decrease generally (Figure 5b). In addition, the model ZC18 with a τ_s/τ_d ratio of 0.15 shows a dually vergent thrust wedge with a weak frontward preferred vergence (Figure 6b), while the model ZC17 with a τ_s/τ_d ratio of 0.17 shows a dually vergent thrust wedge with a backward preferred vergence (Figure 6c). This fact suggests that the

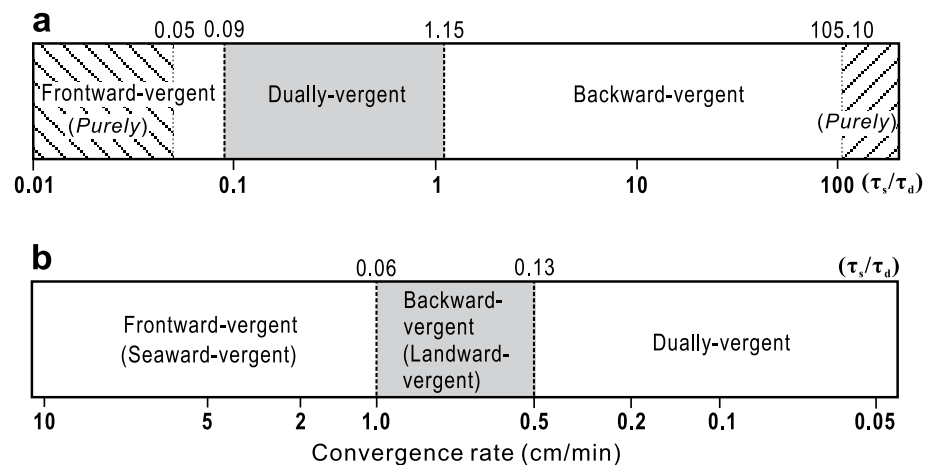


Figure 13. τ_s/τ_d ratio dependence of structural vergence. (a) Results of Type A models, showing that frontward-, dually and backward-vergent thrust wedges occurred when $\tau_s/\tau_d < 0.09$, $= 0.09-1.15$ and > 1.15 , respectively, and that the purely frontward-vergent and purely backward-vergent thrust wedges occurred when the $\tau_s/\tau_d < 0.05$ and > 105 , respectively. (b) Results of the models of Gutscher et al. (2001, based on Figure 4 of theirs), showing that frontward-, dually and backward-vergent thrust wedges occurred when $\tau_s/\tau_d < 0.06$, > 0.13 , and $= 0.06-1.15$, respectively. The τ_s/τ_d ratios were estimated by assuming that in their models the Rhone-Poulenc silicone gel may have a viscosity of 2×10^4 Pa-s, and the frictional coefficient between the quartz sand and the sidewalls and the bulk density of quartz sand may be 0.15 and 1.43 g/cm^3 , respectively.

reversal of preferred vergence in dually vergent thrust wedges may occur at a certain τ_s/τ_d ratio between 0.15 and 0.17.

5.2. Comparisons of Different Models

Up to now, more than two hundred papers of the analogue modeling of thrust wedges have been published on mainstream geoscience journals, but only five of them (Vendeville, 1991, 2007, reported in abstract form; Costa & Vendeville, 2004; Souloumiac et al., 2012; Zhou et al., 2016) explicitly pointed out that direction and magnitude of lateral shear stress may affect the structural vergence and evolution of thrust wedges and less than 10 of these papers concerned the models with two décollements. Except for the models of Zhou et al. (2016), the already published models have rarely been provided with a quantitative estimate of τ_s/τ_d ratio or lateral shear stress. So, it is difficult to compare our models with those already published models at a quantitative level in the context of the relationship between τ_s/τ_d ratio and structural vergence of thrust wedges, thus we had to limit the comparisons of different models mainly among Type A and Type B models, the models of Zhou et al. (2016) as well as the models of Gutscher et al. (2001).

Although both Type A and Type B models show progressive change in structural vergence with the increase of τ_s/τ_d ratio, the τ_s/τ_d ratios for the occurrence of purely backward vergence in the two types of models are very different. Purely backward vergence occurred in Type A models (with one weak décollement) when the τ_s/τ_d ratio reached ~ 105 (Figure 13a), whereas it occurred in the UTS and the LTS of Type B models (with two weak décollements) when the τ_s/τ_d ratio reached only 5.00 (Figure 12) and 15.86 (Figure 9), respectively, much less than that for Type A models. In addition, the τ_s/τ_d ratios for occurrence of frontward vergence in the two types of models are also apparently different. The τ_s/τ_d ratio for the occurrence of frontward vergence in the UTS of Type B models is 0.34 (Figure 9), apparently larger than that (0.09) in Type A models (Figure 13a). This suggests that deformation in adjacent thrust systems at different levels may change the relationship between the τ_s/τ_d ratio and the structural vergence of thrust wedges.

Significant difference in structural vergence can also be observed between the models with different boundary conditions. The model of Zhou et al. (2016) with a front-stop and a back-stop and a τ_s/τ_d ratio of 0.3 shows a backward vergence (see Figure 6d in Zhou et al., 2016), whereas Type A models with similar τ_s/τ_d ratios show a dual vergence (Figure 13a). Similarly, the model of Zhou et al. (2016) with a τ_s/τ_d ratio of 20 shows a dual vergence (Figure 6a in Zhou et al., 2016), whereas Type A models with similar τ_s/τ_d ratios show a typical backward vergence (Figure 13a). This suggests that boundary conditions may influence the relationship between the τ_s/τ_d ratio and the structural vergence of thrust wedges.

The models of Zhou et al. (2016) clearly indicated that different τ_s directions may result in significant differences in the relationship between the τ_s/τ_d ratio and the structural vergence of thrust wedges (for details, see Figure 6 in Zhou et al., 2016). Similar differences may also be observed between the models (base-pull type models) of Gutscher et al. (2001), which have a τ_s with the same direction as the shortening and a rigid backstop with a slope of $\sim 20^\circ$ (see Figure 3 in Gutscher et al., 2001), and our Type A models (back wall-push type models) with a τ_s direction opposite to the shortening direction. Assuming that in Gutscher et al.'s (2001) models the Rhone-Poulenc silicone gel may have a viscosity of 2×10^4 Pa-s (similar to that of the Rhone-Poulenc GS1R gum in Basile & Brun, 1999), and the frictional coefficient between the quartz sand and the sidewalls and the bulk density of quartz sand may be 0.15 and 1.43 g/cm^3 (similar to those in our models), respectively (these parameters have not been provided in their models), the relationship between the τ_s/τ_d ratio and the structural vergence in their models may be estimated as shown in Figure 13b. It is indicated that in Gutscher et al.'s (2001) models frontward-vergent thrust wedges occurred when the τ_s/τ_d ratio is in a range of < 0.06 (Figure 13b), which is comparable to that (< 0.09) in our Type A models (Figure 13a). However, backward-vergent (or landward-vergent) thrust wedges in Gutscher et al.'s (2001) models occurred when the τ_s/τ_d ratio is in a narrow range of 0.06–0.13 (Figure 13b), which is much narrower and less than that (> 1.15) in our Type A models (Figure 13a). Additionally, in Gutscher et al.'s (2001) models dually vergent thrust wedges formed when the τ_s/τ_d ratio is in a wide range of > 0.13 (Figure 13b), whereas in our Type A models they formed when the τ_s/τ_d ratio is in a narrow range of 0.09–1.15 (Figure 13a). In particular, as the τ_s/τ_d ratio increased (or the convergence rate decreased), in our Type A models structural vergence progressively changed from frontward-vergent to dual-vergent and then to backward-vergent, which is compatible with the prediction of Coulomb wedge theory and results of previous analogue models (e.g., Bonini, 2007; Buitter, 2012; Costa & Vendeville, 2002; Huiqi, et al., 1992), whereas in Gutscher et al.'s (2001)

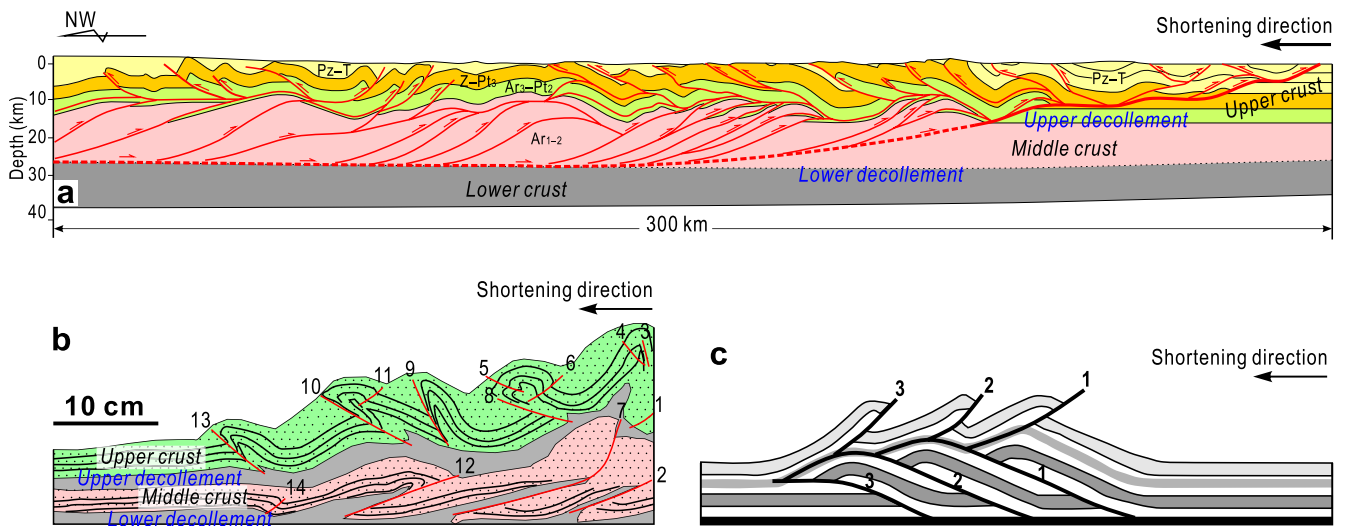


Figure 14. Comparison of Type B model ZC47 with the ESXF TB and passive-roof duplex model. (a) Cross section showing structural features of the ESXF TB (redrawn from Figure 2b). (b) Result of Type B model ZC49 (redrawn from Figure 9e). (c) Passive-roof duplex model (modified by Couzens-Schultz et al. [2003] after Banks and Warburton [1986]).

models structural vergence changed from frontward-vergent directly to backward-vergent, skipping over dual-vergent (Figure 13b).

Additionally, it is worth mentioning that previous models with two décollements also reproduced different structural vergences concurrently at different levels. Their upper and lower thrust systems may have a frontward-, dual- and backward-vergence, respectively (e.g., Bonini, 2001, 2003; Borderie et al., 2018; Couzens-Schultz et al., 2003; Mugnier et al., 1997; Pichot & Nalpas, 2009; Sherkati et al., 2006). But none of them aimed to reproduce a thrust wedge similar to the ESXF TB (Figure 2b), concurrently with a purely backward-vergent lower thrust system and a typical frontward-vergent upper thrust system, because this type of thrust wedges is uncommon in the world.

Above facts suggest that deformation in adjacent thrust systems at different levels, boundary conditions, and direction of lateral shear stress may influence the relationship between the τ_s/τ_d ratio and the structural vergence of thrust wedges. However, due to the lack of sufficient experiments, the influences of these factors as well as the width of model on the relationship between the τ_s/τ_d ratio and the structural vergence of thrust wedges are far from being fully understood and hence further studies are definitely necessary. Our models corroborated that dynamic or origin analysis of thrust wedges should be considered from a 3D perspective (i.e., considering the effect of lateral shear stress). Unlike the 2D dynamic analysis, 3D dynamic analysis of thrust wedges cannot be simply based on the classic Coulomb wedge theory (that considers only a 2D perspective) and the adoption of 2D Mohr diagram, and hence definitely needs adoptions of 3D mechanical analysis tool or software. This work, however, has never been done in previous studies. It would be a special topic of further studies and could be expected to provide a universal explanation for the dynamics or origin of all kinds of thrust wedges.

5.3. Origin of the ESXF TB

Although passive-roof duplex structures, such as those occurring in the Kirthar and Sulaiman fold-thrust belts of Pakistan, the central Canadian Cordilleran fold-thrust belt, and the Amadeus Basin of Australia (Banks & Warburton, 1986; Lebel et al., 1996; Teysier, 1985), may also comprise two oppositely vergent thrust systems that developed concurrently at different crustal levels, their LTS and UTS usually have a typical frontward vergence and a typical backward vergence, respectively (Figure 14c), just opposite to those of the ESXF TB (Figure 14a). Additionally, passive-roof duplexes are usually confined to the front parts of fold-thrust belts, whereas in the ESXF TB the two oppositely vergent thrust systems occupy almost the whole of the fold-thrust belt (Figure 14a). It is therefore indicated that the origin of the ESXF TB cannot be explained simply by the model of passive-roof duplex.

Results of Type B models indicate that in the presence of two weak basal décollements, two thrust systems at different levels may have same, different, and even opposite structural vergences, depending on the combination of different τ_{s1}/τ_{d1} and τ_{s2}/τ_{d2} ratios (Figures 9, 11 and 12). Type B model ZC49 (Figure 14b), which has a τ_{s1}/τ_{d1} ratio of 15.86 and a τ_{s2}/τ_{d2} ratio of 0.34, well reproduced a thrust wedge similar to the ESXFTB (Figure 14a), simultaneously with a purely backward-vergent lower thrust system and a typical forward-vergent upper thrust system (Figure 14b). The result, together with the fact that no evidence for deformation superimposition in the middle crustal thrust system can be observed from the cross section of the ESXFTB (Figure 14a), suggests that the two oppositely vergent thrust systems at different levels in the ESXFTB are not necessarily the products of two opposite shortening events; conversely, they are most likely the results of the single northwestward Mesozoic shortening due to their apparently different τ_s/τ_d ratios.

6. Conclusions

1. The τ_s/τ_d ratio is probably a key factor determining the structural vergence of thrust wedges. Under the condition of one weak décollement, forward-, dually and backward-vergent thrust wedges may occur when the $\tau_s/\tau_d < 0.09$, $= 0.09$ – 1.15 and > 1.15 , respectively. In particular, purely forward- and purely backward-vergent thrust wedges may occur when their $\tau_s/\tau_d < 0.05$ and > 105 , respectively, and the reversal of preferred vergence in dually vergent thrust wedges may occur at a certain τ_s/τ_d ratio between 0.15 and 0.17.
2. Two oppositely vergent thrust systems at different levels can be produced simultaneously in a single shortening process due to their apparently different τ_s/τ_d ratios. The particular structure in the ESXFTB is not necessarily a superposition result of two opposite shortening events but is most likely a product of the single northwestward Mesozoic shortening.
3. The relationship between the τ_s/τ_d ratio and the structural vergence of thrust wedges is far from being fully understood due to the lack of sufficient experiments. Origin or dynamics of thrust wedges should be considered from a 3D perspective and needs adoptions of 3D mechanical analysis tool or software, which could be expected to provide a universal explanation for the origin of all kinds of thrust wedges.

Data Availability Statement

The data supporting the findings of this study are available within the article and its supplementary material. The supplemental information of this work contains additional figures and videos of the models (<https://doi.org/10.6084/m9.figshare.19102760>).

Acknowledgments

This paper benefited significantly from the thorough and constructive comments and suggestions by the two anonymous reviewers, Pauline Souloumiac and Associate Editor Ernst Willingshofer. This work was supported by the Natural Science Foundation of China (grant 41772202). Wenhua Pan helped to do a part of PIV analysis works in this study.

References

- Adam, J., Urai, J., Wieneke, B., Oncken, O., Pfeiffer, K., Kukowski, N., et al. (2005). Shear localisation and strain distribution during tectonic faulting—new insights from granular-flow experiments and high-resolution optical image correlation techniques. *Journal of Structural Geology*, 27, 283–301. <https://doi.org/10.1016/j.jsg.2004.08.008>
- Bahroudi, A., & Koyi, H. (2003). Effect of spatial distribution of Hormuz salt on deformation style in the Zagros fold and thrust belt: An analogue modelling approach. *Journal of the Geological Society*, 160, 719–733. <https://doi.org/10.1144/0016-764902-135>
- Banks, C., & Warburton, J. (1986). ‘Passive-roof’ duplex geometry in the frontal structures of the Kirthar and Sulaiman Mountain belts, Pakistan. *Journal of Structural Geology*, 3, 229–238. [https://doi.org/10.1016/0191-8141\(86\)90045-3](https://doi.org/10.1016/0191-8141(86)90045-3)
- Basile, C., & Brun, J. (1999). Transtensional faulting patterns ranging from pull-apart basins to transform continental margins: An experimental investigation. *Journal of Structural Geology*, 21, 23–37. [https://doi.org/10.1016/S0191-8141\(98\)00094-7](https://doi.org/10.1016/S0191-8141(98)00094-7)
- Bonini, M. (2001). Passive roof thrusting and forelandward fold propagation in scaled brittle-ductile physical models of thrust wedges. *Journal of Geophysical Research*, 106, 2291–2311. <https://doi.org/10.1029/2000jb900310>
- Bonini, M. (2003). Detachment folding, fold amplification, and diapirism in thrust wedge experiments. *Tectonics*, 22, 1065. <https://doi.org/10.1029/2002tc001458>
- Bonini, M. (2007). Deformation patterns and structural vergence in brittle–ductile thrust wedges: An additional analogue modelling perspective. *Journal of Structural Geology*, 29, 141–158. <https://doi.org/10.1016/j.jsg.2006.06.012>
- Bonini, M., Sani, F., & Antonielli, B. (2012). Basin inversion and contractional reactivation of inherited normal faults: A review based on previous and new experimental models. *Tectonophysics*, 522–523, 55–88. <https://doi.org/10.1016/j.tecto.2011.11.014>
- Bonini, M., Sokoutis, D., Mulugeta, G., & Katrivanos, E. (2000). Modelling hanging wall accommodation above rigid thrust ramps. *Journal of Structural Geology*, 22, 1165–1179. [https://doi.org/10.1016/S0191-8141\(00\)00033-x](https://doi.org/10.1016/S0191-8141(00)00033-x)
- Borderie, S., Graveleau, F., Witt, C., & Vendevill, B. (2018). Impact of an interbedded viscous décollement on the structural and kinematic coupling in fold-and-thrust belts: Insights from analogue modeling. *Tectonophysics*, 722, 118–137. <https://doi.org/10.1016/j.tecto.2017.10.019>
- Buiter, S. (2012). A review of brittle compressional wedge models. *Tectonophysics*, 530–531, 1–17. <https://doi.org/10.1016/j.tecto.2011.12.018>
- Byrne, D., Wang, W., & Davis, D. (1993). Mechanical role of backstops in the growth of forearcs. *Tectonics*, 12, 123–144. <https://doi.org/10.1029/92tc00618>

- Byrne, T., & Hibbard, J. (1987). Landward vergence in accretionary prisms: The role of the backstop and thermal history. *Geology*, *15*, 1163–1167. [https://doi.org/10.1130/0091-7613\(1987\)15<1163:lviapt>2.0.co;2](https://doi.org/10.1130/0091-7613(1987)15<1163:lviapt>2.0.co;2)
- Corti, G., Bonini, M., Conticelli, S., Innocenti, F., Manetti, P., & Sokoutis, D. (2003). Analogue modelling of continental extension: A review focused on the relations between the patterns of deformation and the presence of magma. *Earth-Science Reviews*, *63*, 169–247. [https://doi.org/10.1016/s0012-8252\(03\)00035-7](https://doi.org/10.1016/s0012-8252(03)00035-7)
- Costa, E., & Vendeville, B. (2002). Experimental insights on the geometry and kinematics of fold-and-thrust belts above weak, viscous evaporitic décollement. *Journal of Structural Geology*, *24*, 1729–1739. [https://doi.org/10.1016/s0191-8141\(01\)00169-9](https://doi.org/10.1016/s0191-8141(01)00169-9)
- Costa, E., & Vendeville, B. (2004). Experimental insights on the geometry and kinematics of fold-and-thrust belts above weak, viscous evaporitic décollement: Reply to comments by Hemin Koyi and James Cotton. *Journal of Structural Geology*, *26*, 2141–2143. <https://doi.org/10.1016/j.jsg.2004.04.002>
- Cotton, J., & Koyi, H. (2000). Modeling of thrust fronts above ductile and frictional detachments: Application to structures in the Salt Range and Potwar Plateau, Pakistan. *Geological Society of America Bulletin*, *112*, 351–363. [https://doi.org/10.1130/0016-7606\(2000\)112<351:mofad>2.0.co;2](https://doi.org/10.1130/0016-7606(2000)112<351:mofad>2.0.co;2)
- Couzens-Schultz, B., Vendeville, B., & Wiltshko, D. (2003). Duplex style and triangle zone formation: Insights from physical modeling. *Journal of Structural Geology*, *25*, 1623–1644. [https://doi.org/10.1016/s0191-8141\(03\)00004-x](https://doi.org/10.1016/s0191-8141(03)00004-x)
- Cruz, L., Malinski, J., Wilson, A., Take, W., & Hilley, G. (2010). Erosional control of the kinematics and geometry of fold-and-thrust belts imaged in a physical and numerical sandbox. *Journal of Geophysical Research*, *115*, B09404. <https://doi.org/10.1029/2010jb007472>
- Cubas, N., Maillot, B., & Barnes, C. (2010). Statistical analysis of an experimental compressional sand wedge. *Journal of Structural Geology*, *32*, 818–831. <https://doi.org/10.1016/j.jsg.2010.05.010>
- Dahlen, F. (1990). Critical taper model of fold-and-thrust belts and accretionary wedges. *Annual Review of Earth and Planetary Sciences*, *18*, 55–99. <https://doi.org/10.1146/annurev.ea.18.050190.000415>
- Davis, D., Suppe, J., & Dahlen, F. (1983). Mechanics of fold-and-thrust belts and accretionary wedges. *Journal of Geophysical Research*, *88*(B2), 1153–1172. <https://doi.org/10.1029/jb088ib02p01153>
- Dong, S., Zhang, Y., Gao, R., Su, J., Liu, M., & Li, J. (2015). A possible buried Paleoproterozoic collisional orogen beneath central South China: Evidence from seismic-reflection profiling. *Precambrian Research*, *264*, 1–10. <https://doi.org/10.1016/j.jsg.2015.04.003>
- Graveleau, F., Malavieille, J., & Dominguez, S. (2012). Experimental modelling of orogenic wedges: A review. *Tectonophysics*, *538–540*, 1–66. <https://doi.org/10.1016/j.tecto.2012.01.027>
- Gulick, S., Meltzer, A., & Clarke, S. (1998). Seismic structure of the southern Cascadia subduction zone and accretionary prism north of the Mendocino triple junction. *Journal of Geophysical Research*, *103*(B1127), 27207–27222. <https://doi.org/10.1029/98jb02526>
- Gutscher, M., Klaeschen, D., Flueh, E., & Malavieille, J. (2001). Non-Coulomb wedges, wrong-way thrusting, and natural hazards in Cascadia. *Geology*, *29*, 379–382. [https://doi.org/10.1130/0091-7613\(2001\)029<0379:ncwwwt>2.0.co;2](https://doi.org/10.1130/0091-7613(2001)029<0379:ncwwwt>2.0.co;2)
- He, W., Zhou, J., & Yuan, K. (2018). Deformation evolution of Eastern Sichuan–Xuefeng fold-thrust belt in South China: Insights from analogue modelling. *Journal of Structural Geology*, *109*, 74–85. <https://doi.org/10.1016/j.jsg.2018.01.002>
- Huiji, L., McClay, K., & Powell, D. (1992). Physical models of thrust wedges. In K. McClay (Ed.), *Thrust tectonics* (pp. 71–81). Springer. https://doi.org/10.1007/978-94-011-3066-0_6
- Koyi, H., & Vendeville, B. (2003). The effect of décollement dip on geometry and kinematics of model accretionary wedges. *Journal of Structural Geology*, *25*, 1445–1450. [https://doi.org/10.1016/s0191-8141\(02\)00202-x](https://doi.org/10.1016/s0191-8141(02)00202-x)
- Lallemand, S., Schnurle, P., & Malavieille, J. (1994). Coulomb theory applied to accretionary and nonaccretionary wedges: Possible causes for tectonic erosion and/or frontal accretion. *Journal of Geophysical Research*, *99*(B6), 12033–12055. <https://doi.org/10.1029/94jb00124>
- Lebel, D., Langenberg, W., & Mountjoy, E. (1996). Structure of the central Canadian Cordilleran thrust-and-fold belt, Athabasca-Brazeau area, Alberta: A large, complex intercutaneous wedge. *Bulletin of Canadian Petroleum Geology*, *44*, 282–298.
- Lohrmann, J., Kukowski, N., Adam, J., & Oncken, O. (2003). The impact of analogue material properties on the geometry, kinematics, and dynamics of convergent sand wedges. *Journal of Structural Geology*, *25*, 1691–1711. [https://doi.org/10.1016/s0191-8141\(03\)00005-1](https://doi.org/10.1016/s0191-8141(03)00005-1)
- MacKay, M. (1995). Structural variation and landward vergence at the toe of the Oregon accretionary prism. *Tectonics*, *14*, 1309–1320. <https://doi.org/10.1029/95tc02320>
- MacKay, M., Moore, G., Cochrane, G., Moore, J., & Kulm, L. (1992). Landward vergence and oblique structural trends in the Oregon margin accretionary prism: Implications and effect on fluid flow. *Earth and Planetary Science Letters*, *109*, 477–491. [https://doi.org/10.1016/0012-821x\(92\)90108-8](https://doi.org/10.1016/0012-821x(92)90108-8)
- Marques, F., & Cobbold, P. (2002). Topography as a major factor in the development of arcuate thrust belts: Insights from sandbox experiments. *Tectonophysics*, *348*, 247–268. [https://doi.org/10.1016/s0040-1951\(02\)00077-x](https://doi.org/10.1016/s0040-1951(02)00077-x)
- Marques, F., & Cobbold, P. (2006). Effects of topography on the curvature of fold-and-thrust belts during shortening of a 2-layer model of continental lithosphere. *Tectonophysics*, *415*, 65–80. <https://doi.org/10.1016/j.tecto.2005.12.001>
- Mugnier, J., Baby, P., Colletta, B., Vinour, P., Bale, P., & Leturmy, P. (1997). Thrust geometry controlled by erosion and sedimentation: A view from analogue models. *Geology*, *25*, 427–430. [https://doi.org/10.1130/0091-7613\(1997\)025<0427:tgbea>2.3.co;2](https://doi.org/10.1130/0091-7613(1997)025<0427:tgbea>2.3.co;2)
- Pennock, E., Lillie, R., Zaman, A., & Yousaf, M. (1989). Structural interpretation of seismic reflection data from eastern Salt Range and Potwar Plateau, Pakistan. *The American Association of Petroleum Geologists Bulletin*, *73*, 841–857. <https://doi.org/10.1306/44b4a27b-170a-11d7-8645000102c1865d>
- Persson, K., & Sokoutis, D. (2002). Analogue models of orogenic wedges controlled by erosion. *Tectonophysics*, *356*, 323–336. [https://doi.org/10.1016/s0040-1951\(02\)00443-2](https://doi.org/10.1016/s0040-1951(02)00443-2)
- Pichot, T., & Nalpas, T. (2009). Influence of synkinematic sedimentation in a thrust system with two décollement levels; analogue modelling. *Tectonophysics*, *473*, 466–475. <https://doi.org/10.1016/j.tecto.2009.04.003>
- Pons, A., & Mourgues, R. (2012). Deformation and stability of over-pressured wedges: Insight from sandbox models. *Journal of Geophysical Research*, *117*, B09404. <https://doi.org/10.1029/2012jb009379>
- Rossetti, F., Faccenna, C., Ranalli, G., & Storti, F. (2000). Convergence rate-dependent growth of experimental viscous orogenic wedges. *Earth and Planetary Science Letters*, *178*, 367–372. [https://doi.org/10.1016/s0012-821x\(00\)00082-0](https://doi.org/10.1016/s0012-821x(00)00082-0)
- Rossetti, F., Faccenna, C., & Rannalli, G. (2002). The influence of backstop dip and convergence velocity in the growth of viscous doubly-vergent orogenic wedges: Insights from thermomechanical laboratory experiments. *Journal of Structural Geology*, *24*, 953–962. [https://doi.org/10.1016/s0191-8141\(01\)00127-4](https://doi.org/10.1016/s0191-8141(01)00127-4)
- Seely, D. (1977). The significance of landward vergence and oblique structural trends on trench inner slopes. In *Island arcs, deep sea trenches and Back-arc basins* (pp. 187–198). American Geophysical Union. <https://doi.org/10.1029/me001p0187>
- Sherkati, S., Letouzey, J., & Frizon de Lamotte, D. (2006). Central Zagros fold-thrust belt (Iran): New insights from seismic data, field observation, and sandbox modeling. *Tectonics*, *25*, TC4007. <https://doi.org/10.1029/2004tc001766>

- Smit, J., Brun, J., & Sokoutis, D. (2003). Deformation of brittle-ductile thrust wedges in experiments and nature. *Journal of Geophysical Research*, *108*, B2480. <https://doi.org/10.1029/2002jb002190>
- Smit, J., Burg, J., Dolati, A., & Sokoutis, D. (2010). Effects of mass waste events on thrust wedges: Analogue experiments and application to the Makran accretionary wedge. *Tectonics*, *29*, TC3003. <https://doi.org/10.1029/2009tc002526>
- Souloumiac, P., Maillot, B., & Leroy, Y. (2012). Bias due to side wall friction in sand box experiments. *Journal of Structural Geology*, *35*, 90–101. <https://doi.org/10.1016/j.jsg.2011.11.002>
- Teixell, A., & Koyi, H. (2003). Experimental and field study of the effects of lithological contrasts on thrust-related deformation. *Tectonics*, *22*, 1054. <https://doi.org/10.1029/2002tc001407>
- Teysier, C. (1985). A crustal thrust system in an intracratonic tectonic environment. *Journal of Structural Geology*, *7*, 689–700. [https://doi.org/10.1016/0191-8141\(85\)90144-0](https://doi.org/10.1016/0191-8141(85)90144-0)
- Tobin, H., Moore, J., MacKay, M., Orange, D., & Kulm, L. (1993). Fluid flow along a strike-slip fault at the toe of the Oregon accretionary prism: Implications for the geometry of frontal accretion. *Geological Society of America Bulletin*, *105*, 569–582. [https://doi.org/10.1130/0016-7606\(1993\)105<0569:ffaass>2.3.co;2](https://doi.org/10.1130/0016-7606(1993)105<0569:ffaass>2.3.co;2)
- Underwood, M. (2002). Strike-parallel variations in clay minerals and fault vergence in the Cascadia subduction zone. *Geology*, *30*, 155–158. [https://doi.org/10.1130/0091-7613\(2002\)030<0155:spvicm>2.0.co;2](https://doi.org/10.1130/0091-7613(2002)030<0155:spvicm>2.0.co;2)
- Vendeville, B. (1991). Thin-skinned compressional structures above frictional-plastic and viscous décollement layers. *Geological Society of America Abstracts with Programs*, *23*(5), A423.
- Vendeville, B. (2007). The 3-D nature of stress fields in physical experiments and its impact on models overall evolution. *Geophysical Research Abstracts*, *9*, 02960. SRef-ID: 1607-7962/gra/EGU2007-A-02960.
- Yan, D., Zhou, M., Song, H., Wang, X., & Malpas, J. (2003). Origin and structural significance of a Mesozoic multi-layer over-thrust system within the Yangtze block (South China). *Tectonophysics*, *361*, 239–254. [https://doi.org/10.1016/s0040-1951\(02\)00646-7](https://doi.org/10.1016/s0040-1951(02)00646-7)
- Zhang, G., Guo, A., Wang, Y., Li, S., Dong, Y., Liu, S., et al. (2013). Tectonics of South China continent and its implications. *Science China Earth Science*, *56*(1), 1804–1828. <https://doi.org/10.1007/s11430-013-4679-1>
- Zhou, J., Xu, F., Wei, C., Li, G., Yu, F., & Tong, H. (2007). Shortening of analogue models with contractive substrata: Insights into the origin of purely landward-vergent thrusting wedge along the Cascadia subduction zone and the deformation evolution of Himalayan–Tibetan orogen. *Earth and Planetary Science Letters*, *260*, 313–327. <https://doi.org/10.1016/j.epsl.2007.05.048>
- Zhou, J., Zhang, B., & Xu, Q. (2016). Effects of lateral friction on the structural evolution of fold-and-thrust belts: Insights from sandbox experiments with implications for the origin of landward-vergent thrust wedges in Cascadia. *Geological Society of America Bulletin*, *128*, 669–683. <https://doi.org/10.1130/b31320.1>